Radiation Effects on Breast Tissue-Derived Extracellular Matrix Hydrogels

By

Steven M. Alves

Thesis

Submitted to the Faculty of the

Graduate School of Vanderbilt University

in partial fulfillment of the requirements

for the degree of

MASTER OF SCIENCE

in

Chemical Engineering

August 9, 2019

Nashville, Tennessee

Approved:

Marjan Rafat, Ph.D.

John T. Wilson, Ph.D.

Acknowledgements

My greatest thanks goes to those who helped me complete this project. I would like to thank Dr. Marjan Rafat for her guidance during my graduate career, and I would like to thank Dr. John Wilson for his input in completing the project. I am indebted to their support for my critical thinking and academic growth. I would like to acknowledge Tian Zhu, Anastasia Shostak, and Drake Shaub of the ECM team for handling all of our work with enthusiasm, and the lab as a whole for such persistent positivity. Finally, thank you to my parents and family for constantly supporting my decisions, to Julia for coming on this adventure to Nashville, and to my dog Gwen for reminding me to enjoy the simple things.

Table of Contents

List of Tables

List of Figures

CHAPTER I

Introduction

Triple negative breast cancer

Cancer is characterized by an excess of cellular proliferation, evasion of the immune system, and metastasis to distant sites[1]. Over 260,000 women will be diagnosed with breast cancer in 2019, and over 40,000 will die from the disease (Figure 1), making it the second deadliest cancer among women[2]. Triple negative breast cancer (TNBC) is an aggressive subtype that lacks estrogen receptor (ER), progesterone receptor (PR), and HER2. ER and PR are both intracellular, nuclear receptors responsible for initiating transcription of DNA when activated by estrogen and progesterone, respectively[3, 4]. The HER2 receptor is one of four receptors found in the transmembrane human epidermal growth factor family. Basal-like breast cancers are an intrinsic subtype of breast cancer that share many similarities with TNBC. Most basal-like breast cancers are triple negative, and about 80% of TNBC are basal-like[5]. This overlap has led some to use the two names interchangeably for TNBC. Despite these similarities, these cancers cannot be treated as one subtype because basal-like breast cancers occasionally express ER or overexpress HER2, which contradicts the definition of TNBC.

Molecular assays have shown that heterogeneity exists within a tumor of a TNBC patient, which presents a challenge for treatment and often leads to a poor prognosis for the patient[6]. TNBCs can be further divided into groups like claudin-low and interferon-rich. Claudin-low cancers show a cancer stem cell-like phenotype, and interferon-rich cancers overexpress genes normally regulated by interferons[7]. Genetic mutations are a staple of cancer development, and

about 10% of TNBC patients carry mutations on the BRCA1 and BRCA2 genes[8]. The BRCA1 and BRCA2 genes have been shown to play a critical role in repairing DNA damage. They act as tumor suppressor genes and also play a role in cell division and apoptosis[9]. Furthermore, breast cancers with a BRCA1 mutation are likely to carry an additional mutation in the TP53 gene, another tumor suppressor[8]. The heterogeneity and lack of available targets make treating TNBC challenging.

Estimated New Cases

Males				Females		
Prostate	174,650	20%		Breast	268,600	30%
Lung & bronchus	116,440	13%		Lung & bronchus	111,710	13%
Colon & rectum	78,500	9%		Colon & rectum	67,100	8%
Urinary bladder	61,700	7%		Uterine corpus	61,880	7%
Melanoma of the skin	57,220	7%		Melanoma of the skin	39,260	4%
Kidney & renal pelvis	44,120	5%		Thyroid	37,810	4%
Non-Hodgkin lymphoma	41,090	5%		Non-Hodgkin lymphoma	33,110	4%
Oral cavity & pharynx	38,140	4%		Kidney & renal pelvis	29,700	3%
Leukemia	35,920	4%		Pancreas	26,830	3%
Pancreas	29,940	3%		Leukemia	25,860	3%
All Sites	**870,970**	**100%**		**All Sites**	**891,480**	**100%**

Estimated Deaths

Males				Females		
Lung & bronchus	76,650	24%		Lung & bronchus	66,020	23%
Prostate	31,620	10%		Breast	41,760	15%
Colon & rectum	27,640	9%		Colon & rectum	23,380	8%
Pancreas	23,800	7%		Pancreas	21,950	8%
Liver & intrahepatic bile duct	21,600	7%		Ovary	13,980	5%
Leukemia	13,150	4%		Uterine corpus	12,160	4%
Esophagus	13,020	4%		Liver & intrahepatic bile duct	10,180	4%
Urinary bladder	12,870	4%		Leukemia	9,690	3%
Non-Hodgkin lymphoma	11,510	4%		Non-Hodgkin lymphoma	8,460	3%
Brain & other nervous system	9,910	3%		Brain & other nervous system	7,850	3%
All Sites	**321,670**	**100%**		**All Sites**	**285,210**	**100%**

Figure 1: Breast cancer prevalence (adapted from Siegel et al.)[2].

Current standard of care

Despite recent advances in genomics and proteomics, conventional chemotherapy has remained the standard treatment for TNBC patients, as they lack the three key targeting receptors. While primary TNBC tumors exhibit high chemosensitivity, the rate of relapse is high at about 20%[10]. Taxanes and anthracyclines are two common chemotherapies offered to breast cancer patients. Taxanes function by inducing the overproduction of microtubules in cancer cells, disrupting functions necessary for cell survival[11]. Anthracyclines have been proposed to function through several different mechanisms, including DNA damage by free radicals, alkylation, or cross-linking and inhibition of topoisomerase, a nuclear enzyme that assists during the DNA unwinding and rewinding process of DNA replication[12, 13]. Platinum-based neoadjuvant chemotherapies are occasionally given to TNBC patients, but they remain controversial since blood toxicities can arise as a side effect[14].

Targeted therapies provide the possibility of personalized medicine for TNBC patients. Poly(adenosine diphosphate-ribose) polymerase (PARP) inhibitors, mitogen-activated protein kinase kinase (MEK) inhibitors, and phosphoinositide 3-kinase (PI3K) inhibitors have all been recently investigated for treatment. Olaparib, a PARP inhibitor, has recently been approved as a targeted therapy for HER2-negative hormone-receptor positive breast cancer and TNBC[15]. It functions to prevent the repair of DNA double-strand breaks. Since cancer cells replicate more rapidly than normal cells, olaparib preferentially targets cancer cells[15]. MEK inhibitors are being tested for targeting the Ras-MAPK pathway that suppresses tumor-infiltrating lymphocytes in tumors by upregulating the expression of major histocompatibility complex (MHC)-I[16]. Alpelisib, a PI3K inhibitor, has also recently been approved as a targeted therapy for breast cancer, functioning by targeting PI3K in the PI3K/Akt/mTOR pathway[17].

Many women have tumors surgically removed either by mastectomy or lumpectomy followed by radiation treatment. Lumpectomy followed by radiation, also known as breast conversion therapy (BCT), has proven to result in the same long-term survival as mastectomy, which makes it an appealing option due to the reduced invasiveness of the surgery[18]. Radiation is commonly administered in 2 Gy doses to a total of about 50 Gy[19]. Recurrence of breast cancer at the primary tumor site is possible for patients who undergo a mastectomy or BCT, but TNBC patients routinely have the greatest chance of experiencing recurrence[20, 21]. Recurrence may partly be due to circulating tumor cells (CTCs) that escaped the primary tumor and entered the circulatory system before the tumor was surgically removed. It is known CTCs can return to the primary tumor site instead of metastasize to a distant site and that patients with CTCs have a poorer prognosis than patients without CTCs, especially for metastatic breast cancers[22, 23, 24]. It has long been known that ionizing radiation is a carcinogen on breast tissue[25]. Preclinical studies have shown that radiation of normal tissue can cause tumor cell recruitment. Fibrosis, a common radiation-induced change in tissue, is a side effect in which the breast tissue stiffens.

Extracellular matrix (ECM)

The extracellular matrix (ECM) is a complex network of macromolecules that surrounds cells and gives shape, structure, and biochemical and biomechanical properties to tissue[26, 27]. It is composed of functional molecules secreted by cells, resulting in a three-dimensional structure that surrounds the cells, making it unique for each tissue[28]. Major components include collagens, laminin, fibronectin, proteoglycans, and glycosaminoglycans, but relative amounts are dependent on the type of tissue[29]. In breast cancer, collagens I, III, and V are increased while collagen IV is decreased, which is characteristic of the degradation of the basement membrane of the tissue[29]. Laminin-111 is an isoform of laminin that is a major part of the basement membrane and has

been shown to greatly decrease in breast cancer[29]. Laminin-332 production is upregulated in myofibroblasts to promote the survival, migration, and invasion of TNBC cells[30]. Fibronectin is expressed by both cancer-associated fibroblasts and cancer cells[29], and has been shown to be upregulated by resident fibroblasts in metastatic sites[31]. These and other matrix components enable communication between cells and the ECM via biochemical and biomechanical cues (Figure 2). For example, cell-matrix interactions can inactivate apoptosis and induce anti-apoptosis gene expression[32], evade proliferative suppression for continuous growth[33, 34], and induces angiogenesis[35, 36].

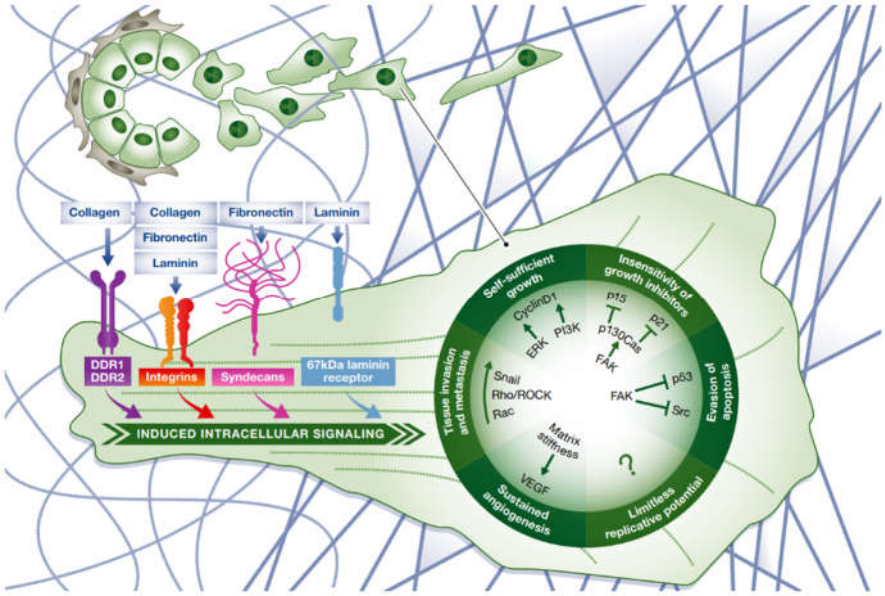

Figure 2: Interaction between cells and the ECM (adapted from Pickup et al.)[37].

The physical properties of the ECM can be altered by malignant cells to enable tumor growth. It is widely accepted that cancer cells exhibit commonalities regardless of the tissue of origin, which are termed the hallmarks of cancer[1]. These hallmarks include a tumor's ability to sustain proliferation, replicate to effectively become immortal, resist cell death, induce

angiogenesis, evade growth suppression, and become invasive. ECM stiffness is a property that contributes toward several of these hallmarks of cancer. It is thought that breast cancer cells can resist apoptosis in a stiff tumor by integrin ligation to the ECM, which can inhibit p53-induced apoptosis[37]. Vascularization to support a growing tumor is associated with increased stiffness. A stiff tumor promotes angiogenesis by upregulating VEGF2 expression, which promotes endothelial proliferation[38]. Metastasis of a malignant tumor type is dependent on ECM stiffness. Several studies have found that tumor metastasis was decreased when collagen crosslinking was inhibited to reduce the matrix stiffness[37]. The ECM is important for tumor cell proliferation because adhesion to the ECM is necessary to complete the cell cycle. Malignant breast tumors are able to supplement the natural ECM by producing their own, which they can use to increase proliferation and become metastatic[34].

Radiation can change the structure and function of ECM. Fibrosis is a result of radiation damage and is the phenomenon of increased fibroblast proliferation and increased ECM deposition[39, 40]. However, this does not imply an increase for all ECM components. For example, the amount of collagen in the ECM has been shown to decrease as an immediate reaction to radiation damage but increase after two weeks[41].

Biomaterials for studying the ECM

Researchers have used several different materials to study the ECM, including both synthetic and naturally derived materials. Polyglycolic acid (PGA) and poly(lactic-co-glycolic acid) (PLGA) are thermoresponsive synthetic materials that are commonly used in the human body for their low toxicity and well-characterized degradation[42, 43]. Thermoresponsivity is an important characteristic for matrix scaffolds because the gel must be injectable for *in vivo* testing. They have both been used to model adipose tissue. Fischbach et al. demonstrated that a

3-dimensional PGA matrix cultured with 3T3-L1 preadipocytes was an improvement over the 2-dimensional PGA matrices that were used up until that point[44]. The 3-dimensional PGA gels were found to macroscopically resemble native adipose tissue when cultured *in vitro*, and the 3T3-L1 cells encapsulated in the gels were able to grow into vascularized fat pads *in vivo*. Patrick et al. showed PLGA scaffold-induced adipogenesis when seeded with primary murine preadipocytes in an *in vivo* model[45]. In the control case without preadipocytes, the PLGA scaffold still induced adipogenesis, though to a lesser extent. Polyethylene glycol diacrylate is another thermoresponsive synthetic material that has been used in adipocyte models and can vary in stiffness, making it a clinical possibility for soft tissue in instances where adipose tissue implants are insufficient[46, 47].

Collagen gels are some of the most common naturally derived gels and have been used for decades to study the ECM. Collagen gels easily gel at physiological temperature because collagen is found throughout the body in the form of fibers. Pins et al. used a collagen I matrix to study the contractile forces on the matrix and the degradation of the matrix when cultured with fibroblasts, finding a connection between ECM degradation and matrix metalloproteinases through the proteinase plasmin[48]. Gentleman et al. showed that collagen fibers derived from bovine Achilles tendon enabled the growth of 3T3-L1 preadipocytes, resulting in mature adipose cells[49]. It was demonstrated that the collagen fibers allowed for a more homogeneous gel than previously reported, making collagen an improved option for soft tissue modeling. Vashi et al. showed that collagen I gel containing fibroblast growth factor-2 (FGF-2) supported the growth of adipose tissue when seeded on a graft in a tissue engineering chamber in the groins of mice[50]. The presence of the fat graft and FGF-2 both promoted adipogenesis, confirming that collagen I alone is insufficient for recapitulating adipose tissue. Starting with a collagen I matrix is

reasonable because collagen I is the most abundant collagen type in the human body[27], but a matrix must contain other proteins for a more accurate representation of the interaction between multiple components.

Matrigel is another common type of ECM hydrogel that has been used for decades to study tissue culture and cell-matrix interactions. Matrigel is primarily made of collagen IV, laminin, and heparin sulfate proteoglycan derived from a murine sarcoma[51], which makes it thermoresponsive, with gelation at physiological temperature. Originating from a mouse, Matrigel cannot be used in humans and still has no direct human equivalent[52]. Kawaguchi et al. demonstrated that Matrigel can be used in combination with basic fibroblast growth factor (bFGF), a signaling protein for the induction of neovascularization, to study adipogenesis[53]. It was found that the Matrigel-bFGF hydrogel was able to promote adipocytes to replace the volume occupied by the gel, which was not the case when Matrigel was tested alone. Cronin et al. showed that Matrigel alone was able to induce an adipogenic response in their flow-through loop pedicle model[54]. Although this model did not supplement the Matrigel with bFGF, the Matrigel was perfused with a major murine leg blood vessel, allowing the gel access to proteins and growth factors normally found in a mouse. Similarly, Kelly et al. used Matrigel to demonstrate the effect of adipogenesis in adipose tissue when in contact with the vasculature[55]. Using this model to build on the work of Kawaguchi et al., it was shown that Matrigel and bFGF together induced angiogenesis but not adipogenesis. A source of adipose next to the model chamber easily induced adipogenesis, further demonstrating Matrigel as a possible model for adipose tissue when used appropriately.

Collagen-hyaluronic acid gels have also been used to study cell-matrix interactions. Hyaluronic acid is an unsulfated glycosaminoglycan present in the ECM of soft tissue, and it has

been shown to play a role in angiogenesis, migration, and differentiation of progenitor cells[56, 57]. Adding hyaluronic acid to collagen gels results in a stiffer hydrogel than either collagen or hyaluronic alone and can better support the growth of chondrocytes and fibroblasts[58, 59]. It has also proven capable of preadipocyte and adipocyte culture and gelling at physiological temperature. Hemmrich et al. demonstrated a soft tissue model of a hyaluronic acid-based sponge in which additional hyaluronic acid resulted in further penetration of human preadipocytes and increasing vascularization compared to a previous model[57]. Campbell et al. used 3T3-L1 differentiated adipocytes cocultured with KIM-2 cells, a type of mammary epithelial cell, to demonstrate mammary organoid formation in a collagen-hyaluronic acid scaffold[60]. Davidenko et al. were able to demonstrate 3T3-L1 differentiation in a collagen-hyaluronic acid model when the cells were given the necessary reagents, and the resulting cells showed upregulated expression of adipogenic genes after one week[61].

Alginate is a naturally occurring polysaccharide found in seaweed that has been used in ECM models. Alginate is composed of alternative blocks of mannuronic acid and guluronic acid, and the guluronic acid blocks can be crosslinked with the addition of divalent cations[62]. Gels based on alginate are thermoresponsive and can be tuned to specific strengths depending on the amount of crosslinking. For example, although alginate can be used for modeling soft tissue, Rowley et al. and Huebsch et al. demonstrated the possibility of recreating an osteogenic environment with arginyl-glycyl-aspartic acid (RGD)-modified alginate[62, 63]. Alginate does not contain mammalian cell binding sites and thus must be modified to promote the adhesion of cells in hydrogels[62]. Chaudhuri et al. used an alginate-Matrigel hydrogel to demonstrate that ECM stiffness and composition influence the phenotype of non-tumorigenic MCF10A cells epithelial cells[64]. In this example, Matrigel contained the necessary components for cell interaction. When

great control over the stiffness of the ECM is desired, alginate stiffness may be modulated based on the amount of divalent cation present.

ECM hydrogels

ECM-derived hydrogels have great potential for study of cell-matrix dynamics and for future therapeutic devices. Derived from primary tissue, the resulting hydrogels are a more accurate representation of the environment that cells encounter. The advantage of using ECM from primary tissue comes from the fact that the ECM is a culmination of proteins secreted by the cells in a given tissue. These proteins serve both structural and functional purposes that promote the continued growth of the cells in a tissue and the shape of the organ[28]. It can be difficult to recapitulate these conditions in conventional synthetic gels or natural gels like collagen. The components of the ECM and their structure are tissue-specific, which would be difficult to mimic in a synthetic or collagen-based gel[65, 66]. The drawback of using ECM hydrogels is the low yield. Adipose cells are large and their lipid content occupies most of that volume. Preparing the ECM for use in hydrogels requires a process called decellularization, in which the cellular contents of a tissue are removed while causing minimal damage to the matrix. Additionally, decellularization of adipose tissue requires delipidation since lipids make up a large volume of the cells. Preservation of the matrix is important for recapitulating the environment seen by cells[67].

There exists a range of decellularization techniques that are dependent on tissue type. All of these techniques involve some combination of chemical, biologic, or physical agents[67]. Detergents are often used in decellularization protocols for removing nucleic acid content and penetrating cell membranes. Sodium dodecyl sulfate (SDS) is one of the most common detergents because it is effective in eliminating the nuclei from dense tissue while preserving

most of the native structure[68]. For thinner tissues, 3-[(3-cholamido-propyl)dimethylammonio]-1-propanesulfonate (CHAPS) has been more effective at preserving the matrix structure. Ionic detergents are quite effective at disrupting the membrane and nucleus, but they nearly always cause some degree of denaturation. Some proteins can be renatured in a lipid environment[69]. Alternatively, Triton X-100 and sodium deoxycholate have proven effective in removing DNA in porcine urinary bladder tissue while better preserving the basement membrane of the ECM[70]. This study involved washing the tissue with Triton X-100 for 24 hours to achieve decellularization, but a shorter exposure of 1 hour can be used to permeabilize the cell membrane, enabling DNA damaging reagents easier access to the nucleus[71]. Additionally, Triton X-100 is a common reagent for membrane permeabilization in a number of assays[72, 73, 74]. Other chemical agents include acids and alcohols. Acetic acid is common for disrupting DNA but can damage collagen and weaken the ECM[75]. Peracetic acid has been used to remove residual nucleic acids after the DNA has been broken down by a reagent that is milder on the matrix than acetic acid. It is effective at concentrations as low as 0.1% v/v, which minimizes ECM damage[76]. Alcohols can also disrupt DNA or remove residual DNA from the matrix. A 75% ethanol/25% acetone solution can disrupt DNA[68], but a dilute solution of 4% ethanol/0.1% peracetic acid can remove nucleic acids after the DNA has been broken down by a reagent that it milder on the ECM[71]. Alcohols are also extremely effective in removing lipid content. Several studies have shown methanol, ethanol, and isopropanol being more effective than lipase in removing lipids[67], but n-propanol has proven effective in delipidation in porcine adipose tissue[71].

Biologics are important in decellularization where chemical agents are ineffective. Nucleases have been used to target DNA in place of detergents, with the advantage being their high specificity[75]. Trypsin is often used for cleaving cells from the matrix by targeting the

carboxyl groups of arginine and lysine at the cell-matrix interface[75]. This technique is widely used, but only for a limited period of time because long exposure to trypsin can cause irreversible damage to the ECM[77]. Ethylenediaminetetraacetic acid (EDTA) is a chelating agent that is often used in combination with trypsin. EDTA aids in dissociating cells from matrix proteins by binding and removing metal ions, possibly enabling trypsin further access to cell-matrix proteins. EDTA alone cannot decellularize tissue, and therefore must be used in combination with trypsin or be followed by another decellularization reagent to be effective[67]. Pepsin is an enzyme found in the porcine gastrointestinal tract that has been used in several protocols to digest the triple helix structure of collagen in the ECM[28]. Lipase may be an alternative for eliminating lipid content, although elimination is incomplete when lipase is used alone. In instances where preservation of the ECM structure is unnecessary, collagenase may be used to intentionally damage collagen within the ECM[67].

Physical agitation can aid in the decellularization of thin tissues, and constant agitation is necessary for denser tissues[75]. Chemical and biologic solutions are more effective when the tissue is submerged and under constant agitation instead of remaining still. Freeze-thaw cycles can also improve the potency of chemical and biologic agents by disrupting cells and having a minimal effect on the mechanical properties of the matrix[75].

Radiation effects on ECM hydrogels of TNBC

An ECM hydrogel model of breast tissue is needed for *in vitro* study of *in vivo* ECM changes as a result of radiation damage. While it is well-known that radiation induces fibrosis in tissue, it has recently been shown that CTCs can return to the primary breast cancer tumor site and reseed in response to radiation[78]. The same researchers then used an immunocompromised model to identify an important cytokine in the return of CTCs to the primary site (Figure 3)[79].

The role of the ECM in influencing recruitment of CTCs and carrying cytokine gradients as a response to radiation damage is still unknown. With the proper ECM hydrogel, the breast tissue cellular environment can be recapitulated in the lab and tested before advancing to more costly *in vivo* studies. A number of adipose ECM hydrogels have been reported in the literature, but they are based on porcine adipose tissue or human lipoaspirate[71, 80]. Additionally, the effect of radiation damage on adipose ECM in a hydrogel model has not been investigated up to this point. The present work describes the development of adipose ECM hydrogels from murine mammary fat pads (MFPs) to evaluate how radiation-induced ECM changes alter tumor cell behavior.

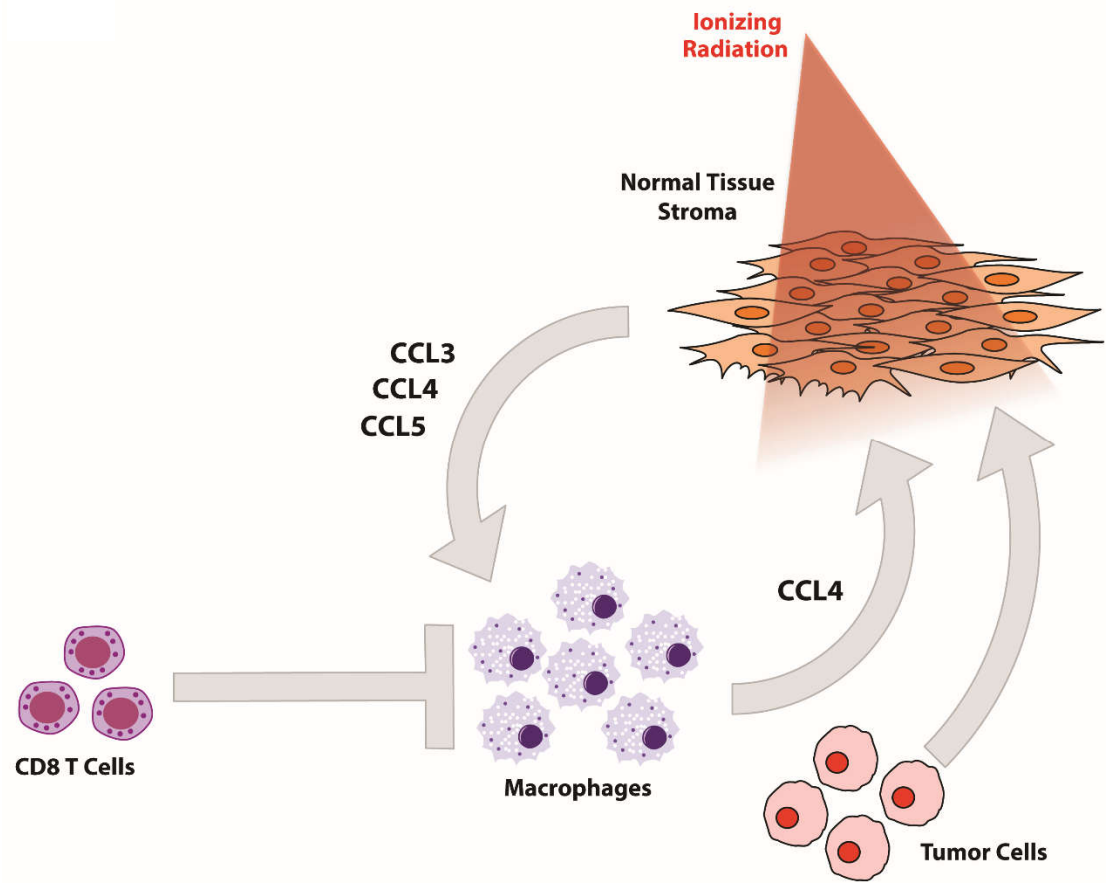

Figure 3: Influence of radiation on tumor cell recruitment to normal tissues (adapted from Rafat et al.)[79].

CHAPTER II

Characterization of ECM Hydrogels

Introduction

Producing hydrogels from soft tissue ECM is a technique that has been used both as an analytical tool and a form of therapy[67, 81, 82]. ECM hydrogels serve as an improvement over conventional synthetic hydrogels because conventional gels fail to replicate the complexities of a tissue's native environment. Collagen I is abundant in tissues but it is not the only component. Matrigel includes growth factors that are generally known to promote cell proliferation, but it is not tissue-specific. ECM has been shown to promote growth of tissue-specific cells for target organs as a result of existing growth factors[83], including *in vitro* and *in vivo* adipogenesis[84, 85]. After decellularization, ECM material is capable of recapitulating the nanostructure and physical properties of tissue, as well as structural and functional proteins, including glycosaminoglycans and proteoglycans[28].

The method of decellularization is an important part of maintaining the integrity of tissue ECM. Methods of decellularization have evolved and been adjusted for different tissue, and the choice of method is critical for ensuring complete decellularization while avoiding permanent ECM damage. The choice of reagents also depends on the tissue itself, which can cause reagents to be more effective or more destructive if the specimen varies greatly in thickness, density, or content[67]. A common decellularization reagent for causing DNA damage is SDS, and it has been used to decellularize adipose[80], cardiac tissue[67], and renal tissue[82] among others. However, SDS can be harsh on tissues and alter structure and organization compared to gentler methods that

often use sodium deoxycholate or CHAPS[74, 86]. Adipose tissue in particular is challenging because adipocytes are largely made of lipid content that cannot be removed with a DNA-damaging reagent. Delipidation can be achieved through alcohol washes, as shown in porcine tissue and skin[71, 85, 87, 88] and human lipoaspirate[89]. Confirmation of decellularization is commonly done through hematoxylin and eosin staining to observe the removal of cell nuclei[68, 84] and Oil Red O staining to observe the elimination of lipids[71, 80].

After decellularization, the subsequent material must form hydrogels to be used in a research or therapy setting. Rheology is a common method for characterizing the physical and mechanical properties of ECM hydrogels[65, 73, 90]. The main outputs are measures of the storage modulus (G') and loss modulus (G'') of the material, which serve as indirect measures of the elastic potential and viscous dissipation, respectively[91]. Gelation is confirmed by demonstrating a storage modulus (G') greater than loss modulus (G'')[92, 93, 94]. Young's modulus, a measure of stress of force per unit area over strain, can be calculated from the storage and loss modulus for comparison to stiffness of normal breast tissue[64].

The following decellularization and hydrogel formation protocol was based on a combination of previous published protocols investigating porcine lungs and human lipoaspirate[71, 80, 95]. The main decellularization process was developed to use Triton X-100 only to permeabilize the cell membranes, sodium deoxycholate over SDS to preserve the murine mammary fat pad tissue structure, and an alcohol wash for delipidation. This method has enabled the study of ECM from murine MFPs.

Methods

Preparation and ex vivo radiation of murine MFPs

Animal studies were performed in accordance with guidelines and protocols approved by the Vanderbilt University Institutional Animal Care and Use Committee. Athymic Nu/Nu mice (8-10 weeks) were sacrificed by carbon dioxide (CO_2) asphyxiation followed by cervical dislocation. MFPs were collected from sacrificed mice using pre-sterilized scissors and forceps in 15 mL conical tubes containing complete RPMI media (RPMI 1640 supplemented with 1% penicillin-streptomycin and 10% fetal bovine serum). Select MFPs were irradiated *ex vivo* to 20 Gy, a dose used to induce radiation damage in previous studies[78, 79], by exposure to a source of cesium-137 while the remaining received 0 Gy (control). MFPs were incubated for two or seven days at 37 °C and 5% CO_2 to promote wound healing and allow the tissue to undergo changes in ECM deposition and remodeling. After incubation, the MFPs were rinsed in phosphate-buffered saline (PBS) and stored at -80 °C overnight in separate 15 mL conical tubes corresponding to their irradiation and incubation status. Final variables tested are seen in Table 1. The shorthand in Table 1 is used from this point onward.

Table 1: MFP variables.

		Incubation time (days)	
		2	7
Radiation dose (Gy)	0	2d 0Gy	7d 0Gy
	20	2d 20Gy	7d 20Gy

Decellularization

MFPs were decellularized after storage at -80 °C for a minimum of 12 hours. MFPs were thawed and weighed, and 2 mm by 2 mm by 2 mm pieces were removed from the tissues using scissors and forceps for hematoxylin and eosin (H&E) staining, Oil Red O staining, and immunohistochemistry (IHC) for a pre-decellularization reference. Pieces saved for H&E staining and IHC were stored in 10% neutral buffered formalin (NBF) for 24 hours, rinsed in PBS, and stored in 70% ethanol until paraffin embedding and sectioning. Pieces saved for Oil Red O staining were submerged in 10% NBF for 24 hours at 4 °C, rinsed 3 times in PBS for 5 minutes each, submerged in 30% sucrose for 48 hours at 4 °C, and frozen in OCT. OCT cassettes containing samples were frozen in 2-methylbutane, which was cooled by liquid nitrogen. Cassettes were stored at -80 °C once the OCT turned from clear to opaque. Decellularization began with MFPs placed in a 6 cm dish containing 5 mL of a 0.02% trypsin/0.05% EDTA solution for 1 hour at 37 °C. Trypsin was used to break extracellular peptide bonds, and EDTA was used to chelate residual metallic ions[67]. The MFPs were then rinsed three times with deionized (DI) water in a strainer and weighed. Between each wash of DI water, the MFPs were manually massaged with forceps. Next, the MFPs were spun in 60 mL of 3% Triton x-100 solution per 1 g of tissue and stirred for 1 hour at room temperature. At that length of time, Triton x-100 was a potent chemical of cell lysis without unnecessary damage to the ECM[70, 71]. The MFPs were again rinsed, massaged, and weighed. Next, the MFPs were spun in 60 mL of 4% deoxycholic acid per 1 g of tissue and stirred for 1 hour at room temperature to disrupt DNA[70]. The MFPs were rinsed, massaged, weighed, and left to sit in 1% penicillin-streptomycin overnight at 4 °C to prevent bacterial contamination. The following day, the MFPs were weighed and then spun in 60 mL of 4% ethanol/0.1% peracetic acid per 1 g of tissue for 2 hours at room

temperature. In dilute solutions, ethanol and peracetic acid are both capable of removing the remaining broken down DNA[71]. The MFPs were rinsed, massaged, and weighed. Finally, the MFPs were spun in 60 mL of 100% n-propanol per 1 g of tissue for 1 hour at room temperature. n-propanol was used for potent delipidation, a major concern considering MFPs are largely made of adipose cells[71]. 2 mm by 2 mm by 2 mm pieces were again removed for H&E staining, Oil Red O staining, and IHC for comparison between normal and decellularized tissue. The remaining tissue was stored in -80 °C for a minimum of 12 hours in a 15 mL conical tube. Table 2 shows the drastic decrease in mass of working material. Over 90% of the mass was removed in all cases.

Table 2: Loss of material by decellularization. Values represent average weight ± standard deviation (SD).

Tissue weight (mg)	Control (0 Gy)	Irradiated (20 Gy)
Initial MFP weight	103.81 ± 40.68	87.96 ± 30.24
After decellularization	5.15 ± 1.97	5.89 ± 2.82
After lyophilization	1.34 ± 0.75	1.24 ± 0.49
Total mass loss (%)	99	99

Lyophilization

Lyophilization is the process of freezing a material, bringing it to vacuum pressure, and sublimating the ice. It has been used in previous adipose tissue decellularization procedures to achieve a brittle material than can be milled into a powder for ECM solution ready for gelation[71,

[80]. Decellularized tissues were removed from -80 °C and placed on dry ice. The 15 mL conical tube caps were replaced with delicate task wipes bound to the conical tube using rubber bands. The tissues were placed on a lyophilizer for 48 hours. The tissues were then returned to dry ice, had the conical tube caps replaced, and were stored at -80 °C for a minimum of 12 hours.

Pregel formation

Lyophilized tissues were removed from -80 °C storage and weighed (Table 2). In a shallow container filled with liquid nitrogen, a hand-held mortar was pre-chilled. Tissues were then milled in the mortar by a pestle attached to a hand-held electric drill. Milling was carried out in 1-minute intervals for a minimum of 5 minutes to achieve the consistency of a powder. Each condition was milled individually. Using the weights of the tissues prior to milling, the necessary amounts of pepsin and hydrochloric acid (HCl) were calculated to achieve a final solution of 1% w/v sample powder and 0.1% w/v pepsin in 0.01 M HCl as has been previously described[95]. Pepsin is a digestive enzyme found in the porcine gastrointestinal tract that breaks down proteins, and HCl was included to activate the enzyme[28]. Pepsin and HCl were combined in a 15 mL conical tube prior to addition of sample powder to ensure that the sample powder was added to a homogeneous solution. Once in solution, the samples were spun with stir bars for 48 hours at room temperature. After 48 hours, the digested solutions were placed on ice for 5 minutes and brought into a biosafety cabinet. A volume of 10x PBS was added to each solution to result in a final concentration of 1x PBS. Finally, 10% v/v 0.1 M sodium hydroxide (NaOH) was added to each solution to reach pH 7.4, resulting in the pregel solution. The pH was tested using pH paper. Raising the pH to pH 7.4 is necessary to inactivate the pepsin. The pregel solutions were stored at 4 °C until use. The resulting solutions corresponded to the conditions in Table 1.

Rheology

Pregel solution was transported on ice for rheological measurements. The rheometer was equipped with a 25 mm diameter plate. Rotational mapping and determining the zero gap of the machine was done at the start of each day. Silicone polymer (Silly Putty) was used to form a basin around the bottom plate. A volume of 500 µL of pregel was pipetted onto the bottom plate at room temperature, and the upper plate was lowered until the liquid spread to occupy the entire space between the plates. When properly occupying the volume, the pregel formed a disc of liquid between the plates. The gap size for all runs was between 900 and 1,000 µm. With the pregel loaded, mineral oil was added to the basin around the bottom plate until the sides of the pregel disc were covered. Submerging the pregel in mineral oil prevented evaporation during long runs.

A time sweep was performed for 60 minutes at constant temperature (37 °C), constant strain (0.5% strain), and constant frequency (1 Hz). Next, a strain sweep was performed from 0% to 2% strain at constant temperature (37 °C) and constant frequency (1 Hz). Finally, a frequency sweep was performed from 0.01 Hz to 3 Hz at constant temperature (37 °C) and constant strain (0.5% strain). All runs were done in triplicate, and all runs were performed after the pregel material had equilibrated to 37 °C. The process was repeated for each pregel solution. For all runs on the rheometer, a storage modulus (G') and loss modulus (G'') was obtained. Young's moduli were calculated using Equation 1:

$$E = 2G(1 + v) \qquad \text{Equation 1}$$

Where

$$G = \sqrt{G'^2 + G''^2}$$

$$E = \frac{\sigma}{\varepsilon}$$

E is Young's modulus, G is shear modulus, G' is storage modulus, G'' is loss modulus, ν is Poisson ratio of the material, σ is stress, and ε is strain. The Poisson ratio was assumed to be 0.5.

Scanning electron microscopy (SEM)

Critical point drying

For a visualization of the effect of decellularization and the structure of the decellularized ECM, hydrogels were formed on glass coverslips. Coverslips were sterilized in an autoclave, brought into a biosafety cabinet, and individually placed into 6-well plate wells. A volume of 50 µL from each pregel solution was deposited onto the sterile coverslips and was incubated for 1 hour at 37 °C to form the hydrogel. Next, the wells were filled with 3 mL of fixative: 2% glutaraldehyde, 4% paraformaldehyde, and 0.1 M sodium cacodylate buffer (pH 7.3). The hydrogels were incubated in fixative for a minimum of 1 hour at 4 °C. Next, the fixative was aspirated, and the hydrogels were washed with 1 mL of 0.1 M sodium cacodylate buffer for 5 minutes at room temperature. Buffer washing was repeated once. Next, the buffer was aspirated, and the hydrogels were submerged in 1 mL of 1% osmium tetroxide (OsO_4) for 1 hour at room temperature. The OsO_4 was aspirated, and the hydrogels were washed with 2 mL of Milli-Q water for 5 minutes. Milli-Q water washing was repeated once. Next, the hydrogels were dehydrated by submergence in 2 mL of 50%, 70%, 90%, 100%, and 100% ethanol solutions for 10 minutes each at room temperature.

Hydrogels on coverslips were brought to a Tousimis Samdri-PVT-3D critical point dryer (CPD) in 100% ethanol. The hydrogels were placed in the CPD holder submerged in 100% ethanol until the machine was ready. The CPD was warmed for a minimum of 3 minutes prior to

use. Once warmed, the liquid CO_2 tank was opened. The chamber was then opened to insert the CPD holder and filled with 100% ethanol prior to securely closing the chamber. The chamber was cooled by opening a valve to bring liquid CO_2 into the machine until the temperature within the chamber reached 0 °C. Once at 0 °C, a valve was opened to fill the chamber with liquid CO_2. The chamber was purged and filled a minimum of three times until the exhaust showed no escaping liquid to ensure complete exchange of ethanol with liquid CO_2. The chamber was filled with liquid CO_2, all valves were closed, and the heater was turned on to begin critical point drying. The machine reached the critical point of CO_2 (1,072 psi, 31 °C) and was maintained for a minimum of 4 minutes. Next, the heater was turned off and pressure was slowly released from the chamber to 400 psi by opening a bleed valve. A separate purge valve was used to release the remaining pressure in the chamber to 0 psi. The chamber was then opened and the tissues were removed. Samples were then placed on carbon tape on a pre-labeled metal stub. Samples were immediately coated with gold-palladium.

Sputter coating

The Cressington Sputter Coater 108 was turned on, and the vacuum inside the chamber was released via a venting knob. The lid was lifted and the chamber was removed so that samples could be inserted. Once the samples were inserted, the chamber was replaced and the lid was closed. A vacuum was pulled using a vacuum pump. An attached argon tank was opened to allow flow to the machine. The vacuum was allowed to approach a pressure of 0.2 mbar in 5-10 minutes. A set knob was used to open the argon gas valve slightly, allowing the pressure to rise to 0.4 mbar for 10 seconds. The set knob was closed to regain and the vacuum. Opening and closing the set knob was repeated until the pressure inside the chamber reached 0.05 mbar. Next,

the set knob was opened to slowly increase the pressure to 0.08 mbar/35 mA, and sputter coating with gold-palladium was started. After 30 seconds, a coating thickness of 178.5 Å coating was automatically stopped. The vacuum pump was turned off, the set knob was fully closed, and the argon tank was closed. The chamber was reopened to retrieve that samples, and the sputter coater was left under vacuum.

Imaging

Imaging was conducted on a Quanta FEG 250 SEM. The microscope chamber vacuum was vented before each opening and pumped after each closing to prevent damage to the machine. All images were obtained at an accelerating voltage of 5 kV and a spot size of 3. FibrilTool, an ImageJ plugin for quantifying alignment, was used to quantify the alignment of hydrogel fibers[96].

Hematoxylin and eosin (H&E) staining

Paraffin-embedded tissues were sectioned at 5 μm onto glass slides by the Vanderbilt University Medical Center Translational Pathology Shared Resource (VUMC TPSR). Slides were deparaffinized and rehydrated, rinsed under running water for 5 minutes, and nuclei were stained with hematoxylin for 3 minutes. The slides were rinsed under running water for 5 minutes and then differentiated in a 0.3% acid alcohol (2 dips) solution to reduce excess background staining for the hematoxylin. Slides were rinsed under running water for 5 minutes, a bluing agent was added for 30 seconds to stop differentiation, and slides were rinsed again. The slides were then dehydrated with 95% ethanol for 30 seconds, counterstained with eosin for 90 seconds, and then dehydrated in 3 changes of 100% ethanol. Slides were then dipped in two

100% xylene solutions for 5 minutes each and then mounted with DPX (distyrene, a plasticizer [tricresyl phosphate], and xylene).

Oil Red O staining

A 0.5% Oil Red O solution was prepared prior to staining. Immediately before staining, Oil Red O solution was filtered with a 0.45 μm filter. 5 μm and 30 μm section slides of normal and decellularized MFPs that had incubated in sucrose were dipped in 100% propylene glycol for 2 minutes and then immediately placed into Oil Red O solution for 2 hours at room temperature. Slides were then differentiated in 85% propylene glycol for one minute, rinsed twice with PBS, and stained with hematoxylin for 1 minute. The slides were then rinsed twice with DI water and coverslipped with the aqueous-based mounting medium Fluoromount-G.

Immunohistochemistry

5 μm sections of paraffin-embedded tissues were made by the VUMC TPSR and mounted on glass microscope slides. Slides were first dewaxed in xylene and rehydrated in ethanol baths of decreasing concentrations of ethanol until reaching 100% DI water. Next, slides were heated in a container of 10 mM citric acid at pH 6 with 0.05% Tween 20 by a 95-100 °C water bath. Slides were heated for 30 minutes to make the antigen presentable to forthcoming antibodies and then cooled for 30 minutes. Slides were then washed in PBS three times for 5 minutes each. Next, slides were submerged in 35% hydrogen peroxidase for 10 minutes at room temperature, which reduced endogenous peroxidase activity of the cells in the sample and eliminated background during the future horseradish peroxidase (HRP) step. Next, slides spent 1 minute in DI water and then the PBS wash was repeated. An ImmEdge hydrophobic barrier pen

was used to draw around the samples to limit the amount of antibody needed to cover the samples. Next, slides were submerged in 1% Tween 20 in PBS to permeabilize the membranes of the cells in the sample. Then the slides were blocked with 10% normal goat serum for 1 hour at room temperature to reduce non-specific staining. Next, the samples were covered with avidin for 15 minutes and then rinsed in PBS three times for 30 seconds each. Slides were then covered with biotin for 15 minutes and then rinsed in PBS three times for 30 seconds each. Avidin blocked endogenous biotin, and then biotin was added to amplify the signal. Slides were covered with a primary antibody and left overnight at 4 °C. The primary antibodies included rabbit anti-mouse collagen I, rabbit anti-mouse collagen IV, rabbit anti-mouse fibronectin, and rabbit anti-mouse laminin. The following day, slides were washed in PBS three times for 5 minutes each. Slides were covered with a secondary antibody for 1 hour at room temperature to amplify the signal of the primary antibody and washed again in PBS three times for 5 minutes each. Next, slides were covered with biotin and streptavidin conjugated to HRP for 45 minutes at room temperature to further amplify the signal. The slides were washed in PBS three times for 5 minutes each. Next, 3,3'-diaminobenzidine tetrahydrochloride (DAB) in HRP solution was added to the slides and monitored closely. DAB was used to visualize positive staining by changing to a brown color when bound to HRP. Slides were placed in DI water as soon as brown was visible to quench the reaction. The samples were covered with hematoxylin for 10 seconds to stain nuclei and visualize cells. Slides were gently rinsed by a slow stream of running tap water and were then dehydrated by a 75% ethanol bath, a 95% ethanol bath, and finally a 100% ethanol bath. Dehydrated slides were covered with DPX mountant, and a coverslip was applied. Staining was imaged under a brightfield microscope, and analysis was conducted in ImageJ by

subtraction of background staining, conversion to a binary image, and quantification of the resulting positive staining.

Results

Characterization of the hydrogels revealed that radiation plays a role is changing the morphology and physical properties of adipose ECM hydrogels. H&E staining of MFPs prior to decellularization demonstrated normal adipose tissue structure (Figure 4A-D). Decellularization collapsed the structure as expected due to the removal of adipocytes. A decrease in nuclei was seen in all conditions after decellularization, confirming decellularization (Figure 4E-H). Oil Red O staining confirmed delipidation of the tissue (Figure 4I-K). An unirradiated MFP sample demonstrated the effect of delipidation, but the sample showed the same deformity seen in the H&E staining as a result of decellularization (Figure 4I, J). All H&E and Oil Red O sections were cut in 5 μm sections, except Figure 4K, which was an unirradiated MFP sample prior to decellularization that was cut at 30 μm. The sectioning technique or the Oil Red O procedure was suspected of changing the adipose morphology due to the excess Oil Red O in Figure 4I. The thicker section confirmed lipid staining.

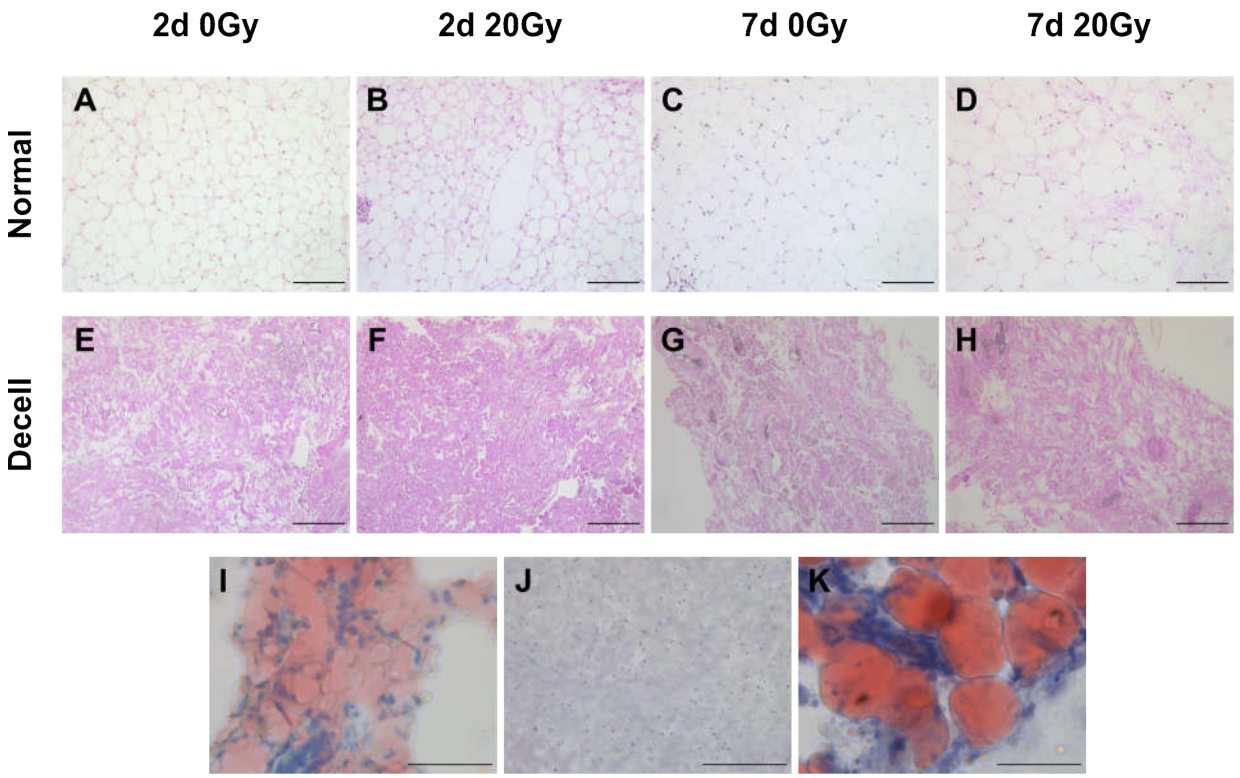

Figure 4: Histology of decellularization. A-H: H&E staining of 5 µm sections before and after decellularization. Nuclei were apparent in normal tissue (A-D) and were not visible in decellularized tissue (E-H) regardless of MFP radiation exposure. I-K: Oil Red O staining of 5 µm sections before and after decellularization (I, J) and a 30 µm section before decellularization (K). Lipids were visibly eliminated after delipidation (before: I, after: J). A thicker section revealed positive lipid staining with adipose cells maintaining morphology. Scale bars of A-H: 100 µm. Scale bars of I-K: 50 µm. Representative images C, D, G, H: N = 3. Remaining images: N = 2.

IHC was performed to see the effect of decellularization and radiation on ECM components, and it revealed that the decellularization process did not remove key ECM components as expected. Figure *5* shows positive staining for four ECM components, and Figure

6 shows the results of IHC staining for collagen I, collagen IV, fibronectin, and laminin. Collagen I was increased as a result of decellularization for MFPs that were irradiated for 7 days after irradiation, with one condition showing a statistically significant increase of over 150%. Collagen IV also increased after decellularization for the MFPs that were incubated for 7 days after irradiation. The remaining of conditions did not significantly change as a result of decellularization.

Ex vivo irradiation minimally altered the ECM components as analyzed by IHC. A trending decrease in collagen I of 22% and 36% was seen in both normal and decellularized MFPs that were incubated for 2 days following irradiation, respectively. That decrease was no longer observed after 7 days of incubation. Collagen IV showed no difference after 2 days of incubation, but after 7 days of incubation, both normal and decellularized MFPs showed a trending increase in response to radiation. Decellularized MFPs that were incubated for 2 days and normal MFPs that were incubated for 7 days showed a trending increase in fibronectin, while decellularized MFPs that were incubated for 7 days showed a trending decrease in fibronectin. An increasing trend in laminin was found in both normal and decellularized MFPs that were incubated for 2 days, while decellularized MFPs that were incubated for 7 days showed a trending decrease in laminin.

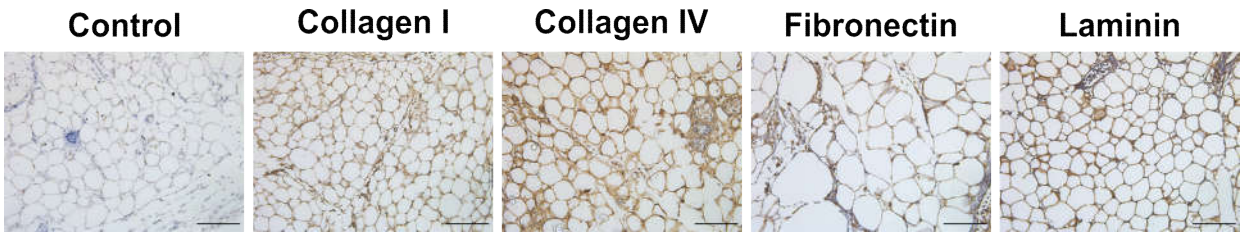

Figure 5: IHC staining of ECM components. Representative images of a control and positive staining for collagen I, collagen IV, fibronectin, and laminin. Scale bars: 100 μm. N = 3.

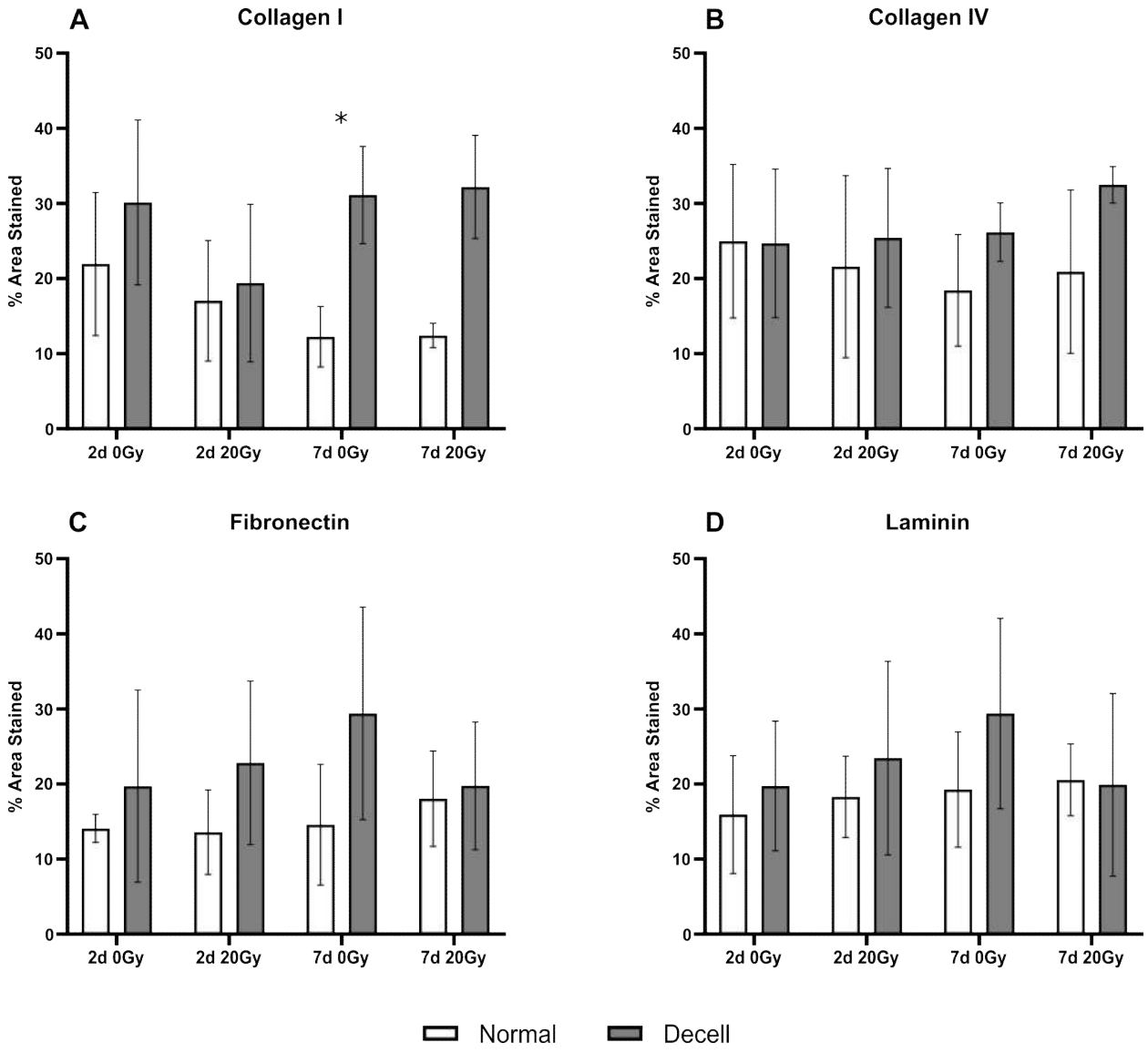

Figure 6: ECM components in response to decellularization and radiation. Percent area of positive staining of collagen I (A), collagen IV (B), fibronectin (C), and laminin (D). Error bars represent SD. Two-tailed Student's *t*-test, $*p < 0.05$. N = 3.

Rheology confirmed the formation of a gel-like material based on storage modulus maintaining a value greater than loss modulus after a time sweep[92] (Figure 7A-D). Young's

modulus was calculated using Equation 1 and data from the last 10 minutes of each time sweep. The results are seen in Table 3. The hydrogels were found to be in the linear elastic regime and show strain dependence (Figure 7E-H) and frequency dependence (Figure 7I-L) similar to other decellularized adipose tissue pregels[64]. Time sweep rheology showed similar storage and loss moduli for the pregels derived from MFPs incubated for 2 days, regardless of radiation exposure. MFPs that were incubated for 7 days following irradiation showed a marked decrease in storage modulus compared to the equivalent control and when compared to the other irradiated condition in which the MFP was incubated for 2 days (Figure 7D). This indicated that self-healing mechanisms of *ex vivo* radiation damage within the MFPs were time dependent.

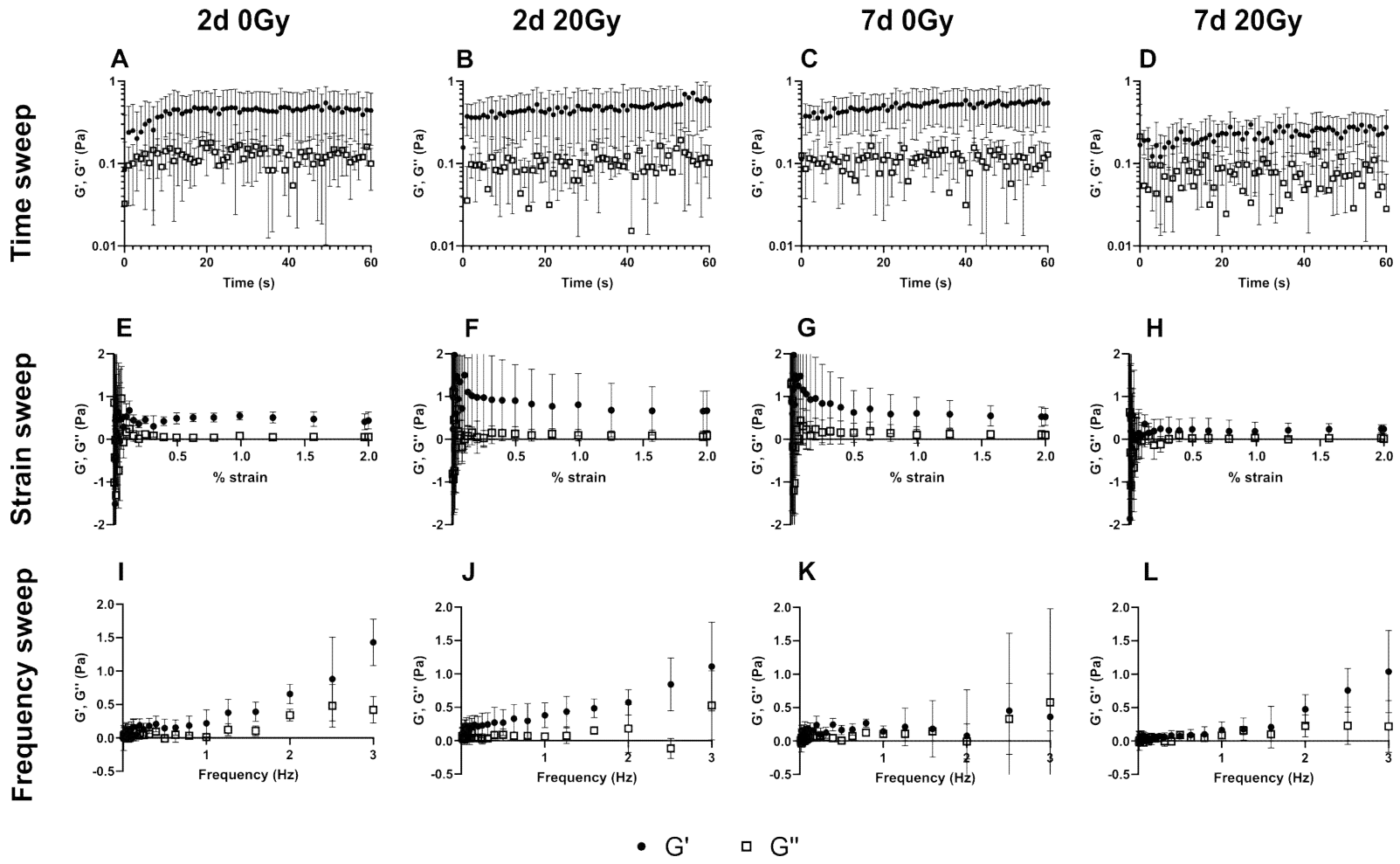

Figure 7: Rheology of hydrogels. Time sweeps (A-D), strain sweeps (E-H), and frequency sweeps (I-L). Error bars represent SD.

Time and strain sweeps: N = 4. Frequency sweeps: N = 3.

Table 3: Young's moduli of hydrogels. Values represent the average of the last 10 minutes ± SD. N = 3.

2d 0Gy (Pa)	2d 20Gy (Pa)	7d 0Gy (Pa)	7d 20Gy (Pa)
0.469 ± 0.265	0.609 ± 0.336	0.563 ± 0.294	0.271 ± 0.138

The morphology of the ECM hydrogels varied depending on MFP incubation time and radiation. SEM images revealed a noticeable morphological change in ECM structure of pregel derived from the unirradiated MFPs incubated for 7 days (Figure 8A-H). The ECM structure appeared flatter and the fibers appeared thicker than the equivalent irradiated condition, which resembled both of the conditions derived from MFPs incubated for 2 days. A similar trend was found quantitatively by anisotropic measurement of the ECM fibers. Anisotropy is a measure of directional dependence, or the degree of alignment, of a material property based on a set of variables. With the tool used in this method, 0 corresponds to an array of fibers with no order and 1 corresponds to perfectly ordered fibers. In this case, the variables are the incubation time and radiation exposure. The ECM derived from unirradiated MFPs incubated for 7 days showed the lowest degree of anisotropy, while the others had relatively equal levels of anisotropy (Figure 8I).

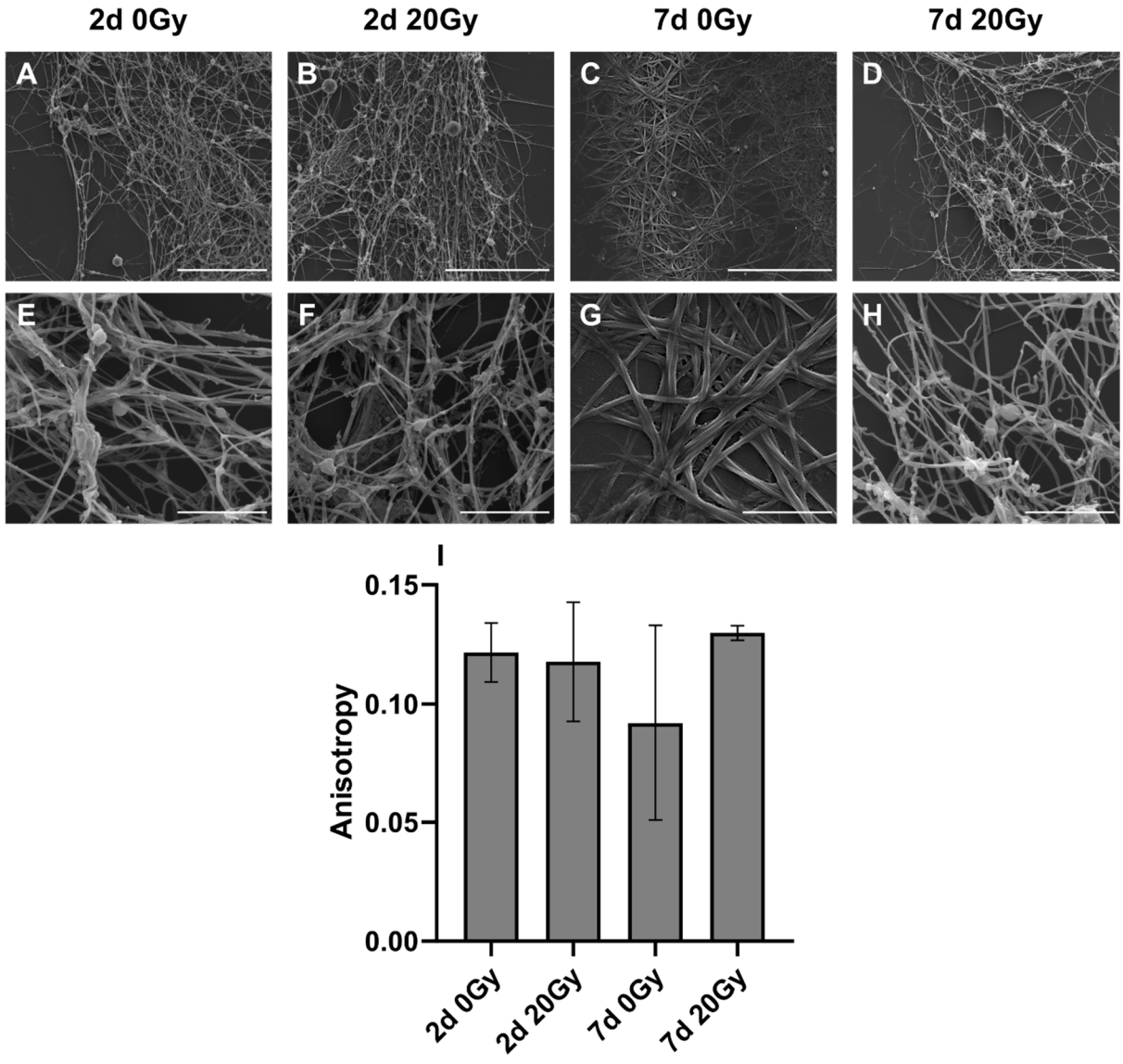

Figure 8: Hydrogel structure and alignment. SEM images at 10,000x magnification (A-D) and 50,000x magnification (E-H). Anisotropy of ECM hydrogel fibers at 50,000x magnification (I). Scale bars of A-D: 10 µm. Scale bars of E-H: 2 µm. Error bars represent SD. Representative images: N = 3. Anisotropic data: N = 2.

Discussion

The decellularization process proved effective, but the hydrogel formation gave unexpected results. Histology confirmed decellularization and delipidation of tissue while deforming the ECM. Adipose cells are large and globular, with lipids occupying most of their volume. Delipidation likely caused the deformation by allowing the ECM to occupy the volume that was previously occupied by lipids. The changes in morphology observed in Figure 4 have been seen by other researchers[89], which indicates this is an inherent characteristic of adipose tissue. Young et al. used the same stains to demonstrate that this deformation occurs as a result of delipidation as opposed to the other parts of a decellularization procedure[80]. An increase in collagen I was seen in samples after 7 days of incubation. This may be explained by the effect of the incubation time prior to decellularization. Qualitatively, it has been demonstrated that decellularization of adipose tissue may increase the collagen I content within the ECM[71, 80]. Quantitatively, it has been reported that decellularization of adipose tissue is capable of increasing collagen via a hydroxyproline assay, which measures total collagen content[84].

We evaluated collagen I, collagen IV, laminin, and fibronectin as they are prominent components of adipose ECM[29]. While our analysis did not reveal significant differences in these components following radiation or decellularization, these experiments were limited by tissue loss at each processing step, which reduced the available material for IHC staining. Future experiments will examine additional tissues with larger surface areas to more accurately evaluate ECM components following irradiation.

The resulting ECM hydrogels were mechanically softer than expected. The Young's moduli of normal breast tissue ranges from 90-945 Pa, but Table 3 shows that none of the hydrogels achieved 1 Pa[64]. Despite the low Young's moduli, time sweeps showed that the

hydrogels were capable of maintaining a gel-like material with a storage modulus greater than a loss modulus (Figure 7A-D). It has been reported that a porcine bladder ECM hydrogel may vary in storage modulus between 5-25 Pa depending on the concentration of ECM in the resulting hydrogel[76], which may explain the low storage moduli in the current hydrogels. The porcine bladder ECM was digested in a pepsin solution such that it contained 1% w/v ECM powder. The same concentration was used for the current hydrogels, but using adipose tissue likely resulted in a softer hydrogel as an inherent trait of the tissue.

The morphology of most hydrogels appeared similar to previously reported SEM images of decellularized adipose tissue (Figure 8A-H)[80, 89]. The structure is fibrillar and has depth, further confirming the presence of a hydrogel. The exception to this was the hydrogel derived from unirradiated MFPs that were incubated for 7 days, suggesting that radiation damage promoted ECM deposition. After 2 days of incubation, no change was found as a result of radiation tissue damage. After 7 days of incubation, the irradiated MFPs may have responded on a cellular level against the damage by depositing ECM despite incubating *ex vivo*, which is indicative of fibrosis in the tissue[40]. We did not, however, observe these changes using IHC. The discrepancy may be due to the presence of other components in the ECM, the sensitivity of the IHC method, or the lack of sufficient material to comprise representative samples as described above. It is possible that these key components remained while the ECM lost structure as a result of sitting *ex vivo* for 7 days without a stimulus, which may have led to a decrease in ECM fiber alignment (Figure 8I).

CHAPTER III

Cellular Interactions with ECM-derived Hydrogels

Introduction

The ECM plays a major role in regulating cell behavior. Largely made of collagen, fibronectin, laminin, and glycosaminoglycans and proteoglycans, ECM regulates the differentiation, proliferation, and migration of cells throughout tissue[37, 97], influences the differentiation of endothelial cells in close proximity, and influences immune activity[98]. In breast tissue, the ECM has additional responsibilities, including the progression of breast development[99], and the regulation of lactation and involution before and after pregnancy[98]. Changes to the ECM can influence the behavior of cells and vice versa. Fibrosis is a common result of excess cellular deposition of collagen I, which is the largest component of ECM[29], but fibrosis can also result from cellular deposition of other ECM components like fibronectin[98]. In solid tumors, the ECM continues to play a major role. Tumors are known to have increased ECM deposition and to become stiffer as the tumor progresses[98, 100, 101]. Increased ECM stiffness may enhance cancer cell invasiveness or expression of ECM-destructive MMPs[102]. This increased stiffness can make treatment difficult by inducing hypoxic regions that can become resistant to therapy[98].

Radiation treatment is a form of therapy that has drastic impacts on the ECM. It has been shown that radiation induces fibrosis, likely through increased pro-inflammatory cytokines like TGFβ that promote fibroblast proliferation[39, 103, 104]. Recently, is has been shown that radiation to the primary site of a resected tumor can promote recurrence to the primary site, especially in

TNBC[20, 78, 79]. Changes to the ECM at the primary site, like fibrosis, seem to create an environment that is suitable for recurrence, and radiation seems to influence circulating tumor cells back to that site.

Previous work has been published on adipose ECM hydrogels. Most researchers have used porcine adipose tissue or human lipoaspirate due to their abundance. Previous hydrogel formation protocols have used GFP-labeled cells to visualize movement and growth through hydrogels[94, 105, 106], and the F-actin within cells has been used to observe the cellular cytoskeleton[84]. Quantitatively, luciferase-labeled cells are commonly used in *in vivo* models for cell tracking and for a method of cell counting[22, 79]. In this study, murine TNBC 4T1 cells were cultured in ECM hydrogels. Changes in proliferation and cell morphology were observed as a function of MFP incubation time and radiation exposure.

Methods

Cell culture

4T1 cells were grown for encapsulation in hydrogels. 4T1 cells are a metastatic strain of murine TNBC that has been used to study the effects of radiation on breast tissue[79]. One line was labeled with GFP and luciferase, and a second line was unlabeled. Cells were grown to 70-80% confluence, pelleted, and resuspended in pregel solution at a concentration of 100,000 cells/mL pregel solution and 500,000 cells/pregel solution. GFP- and luciferase-labeled 4T1 cell-pregel solution was deposited into the wells of 16-well chamber slides at volumes of 30 µL or 50 µL. Unlabeled 4T1 cell-pregel solution was deposited into the wells of 16-well chamber slides and a 96-well plate at volumes of 30 µL or 50 µL The chamber slides and plate were incubated for 30

minutes at 37 °C to induce gelation. A volume of 100 µL of complete RPMI media was then added to each well. The hydrogels were incubated for 48 hours at 37 °C.

Fluorescence imaging

Hydrogels seeded with GFP- and luciferase-labeled 4T1 cells were imaged at 0, 24, and 48 hours following the addition of 100 µL of RPMI media. The GFP label on the cells enabled visualization of proliferation in the hydrogel over time. Cells were visible at an excitation/emission of 488/520 nanometers (nm). The same hydrogels were then measured on the In Vivo Imaging System (IVIS).

In Vivo Imaging System measurements

After the 48-hour fluorescence imaging time point of the GFP- and luciferase-labeled 4T1 seeded hydrogels, luciferin was added to a final concentration of 167 µg/mL. The mixture was incubated for 10 minutes before luminescence imaging on an IVIS. The same regions of interest (ROIs) were used for all experiments for consistency.

Viability assay

An Invitrogen Molecular Probes LIVE/DEAD Viability/Cytotoxicity Kit for Mammalian Cells was used to investigate the cytotoxicity of the ECM hydrogels. After culturing unlabeled 4T1 cells for 48 hours in hydrogel, the remaining liquid was aspirated off the surface of the hydrogels in both the 96-well plate and 16-well chamber slide. Dulbecco's PBS (DPBS) was added to each well and then aspirated to rinse the cells. A volume of 100 µL of DPBS containing 1 µM calcein acetoxymethyl (AM) and 2 µM ethidium homodimer was added to each well and

incubated for 30 minutes at room temperature. Calcein AM is capable of entering live cells and was used to visualize live cells by fluorescing as a result of intracellular esterase activity. Ethidium homodimer is capable of entering dead cells with permeabilized membranes and was used to visualize dead cells by fluorescing as a result of binding to nucleic acids[107]. The 16-well chamber slide was imaged on a fluorescent microscope, and the 96-well plate was read on a plate reader. For both, calcein AM was observed at excitation/emission of 494/517 nm. Ethidium homodimer was observed at excitation/emission of 528/645 nm. Viability was calculated as the live cell counts over the sum of the live cell counts and dead cell counts for a live percentage.

F-actin stain

After culturing GFP- and luciferase-labeled cells for 48 hours in hydrogel, the cells were stained with phalloidin conjugate to visualize the F-actin cytoskeleton. The remaining liquid was aspirated off the surface of the hydrogels in the 16-well chamber slides, and PBS was added and then aspirated to rinse the wells. A volume of 200 µL of 10% NBF was added to the wells and incubated for 20 minutes at room temperature. Next, the NBF was aspirated, and the wells were washed with PBS three times. A single wash consisted of the wells sitting with a volume of 200 µL of PBS for 5 minutes followed by aspiration of the liquid. Next, 200 µL of 0.1% Triton x-100 in PBS was added to the wells and incubated for 5 minutes at room temperature. The wells were then washed with PBS three times. Next, 100 µL of the working solution was added to the wells and incubated for 1 hour at room temperature in the dark. The working solution consisted of 1000x phalloidin conjugate (iFluor 594 dye) diluted to 1x in PBS with 1% bovine serum albumin (BSA) and 20 mM Hoechst 33342 diluted to 0.002 mM. Phalloidin conjugate was used to stain

for F-actin filaments, and Hoechst 33342 was used to visualize cells by staining nuclei. The wells were then washed with PBS three times.

To image the slides, the PBS was aspirated, the chamber was removed, and the gasket holding the chamber to the slide was removed. Fluoromount-G mounting medium was applied and a coverslip was added. The mounting medium was left to cure for a minimum of 5 minutes. Finally, the slide was imaged under a fluorescent microscope at excitation/emission of 590/618 nm to visualize the actin filaments and an excitation/emission of 361/497 nm to visualize the nuclei. FibrilTool was used to quantify the alignment of F-actin. Images of phalloidin conjugate staining were merged with images of nuclei staining in ImageJ to determine the locations of cells. The channel of the phalloidin conjugate stain was quantified by using the polygon tool to outline the borders of cells and FibrilTool to quantify anisotropy.

Results

In vitro culturing of murine TNBC cells in MFP ECM hydrogels showed the effect of irradiated ECM hydrogels on the morphology and proliferation of embedded cells (Figure 9). GFP images of the hydrogels 48 hours after inoculation showed similar amounts of proliferation in both irradiated and control conditions regardless of incubation time, cell seeding concentration, or cell-pregel seeding volume. One exception was found between Figure 9B and Figure 9F and Figure 9J and Figure *9*N, where radiation may have increased proliferation. This indicates that seeding density may influence cell-matrix interactions. A seeding concentration of 500,000 cell/mL was considered a maximum based on preliminary experiments to prevent the cells from becoming overconfluent after 48 hours.

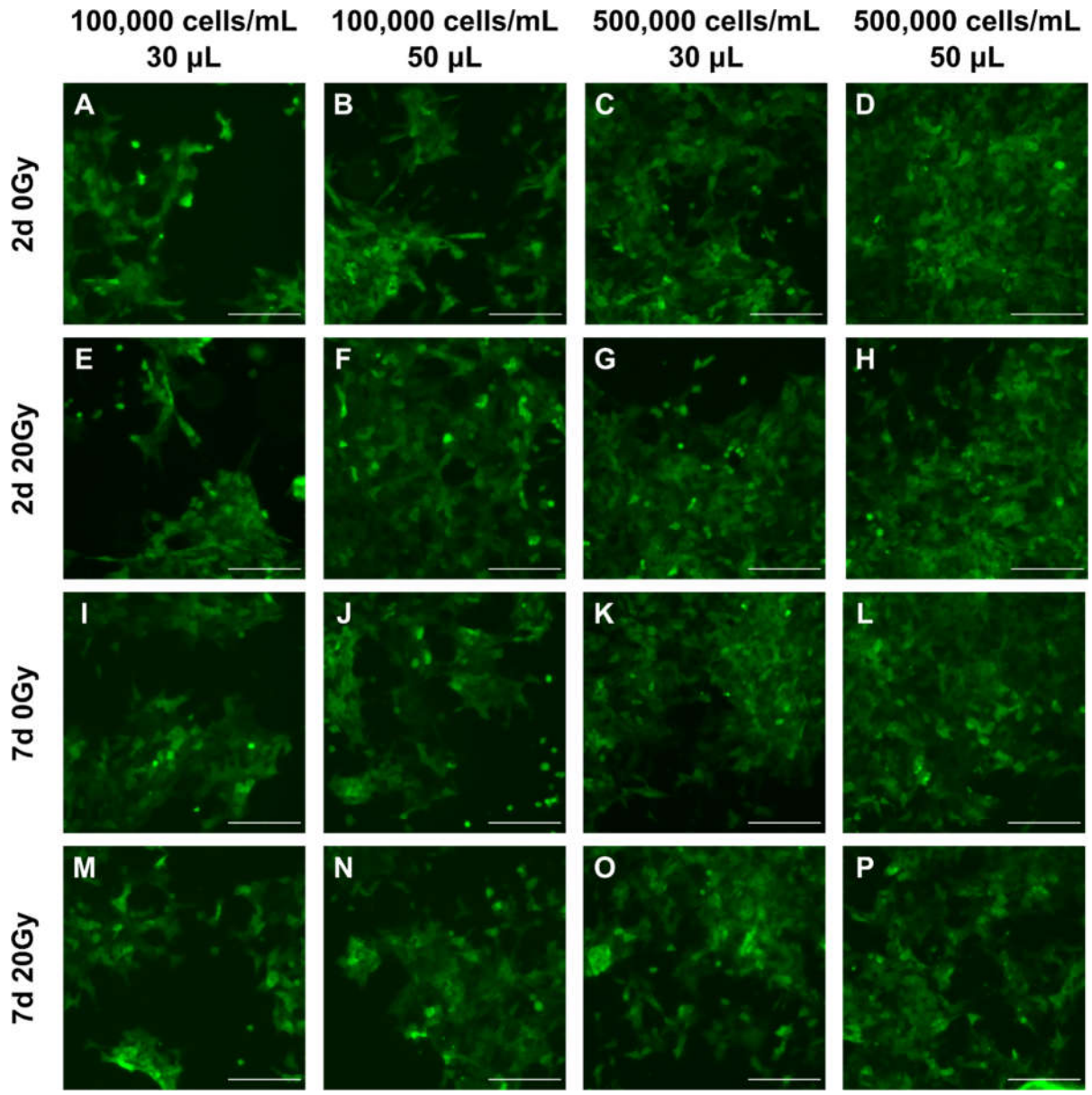

Figure 9: Proliferation of 4T1 cells in ECM hydrogels. Representative images of GFP- and luciferase-labeled 4T1 cells at 48 hours after gelation. Scale bars: 200 µm. A-H, J-P: N = 2. I: N = 1.

Bioluminescent measurements revealed increasing trends in proliferation in hydrogels derived from irradiated MFPs following 2-day incubation when seeded with a lower cell

concentration, though these differences were not statistically significant (Figure 11). Differences in the volumes of cell-pregel solution, which alters cell density, had a lesser impact. The hydrogels seeded at the higher concentration remained consistent throughout, indicating that the effect of radiation on the decellularized ECM may have been overpowered by the number of cells seeded. A viability assay showed that the ECM hydrogels were not cytotoxic to 4T1 cells (Figure 11A, B) with over 95% viability in all conditions (Figure 11C).

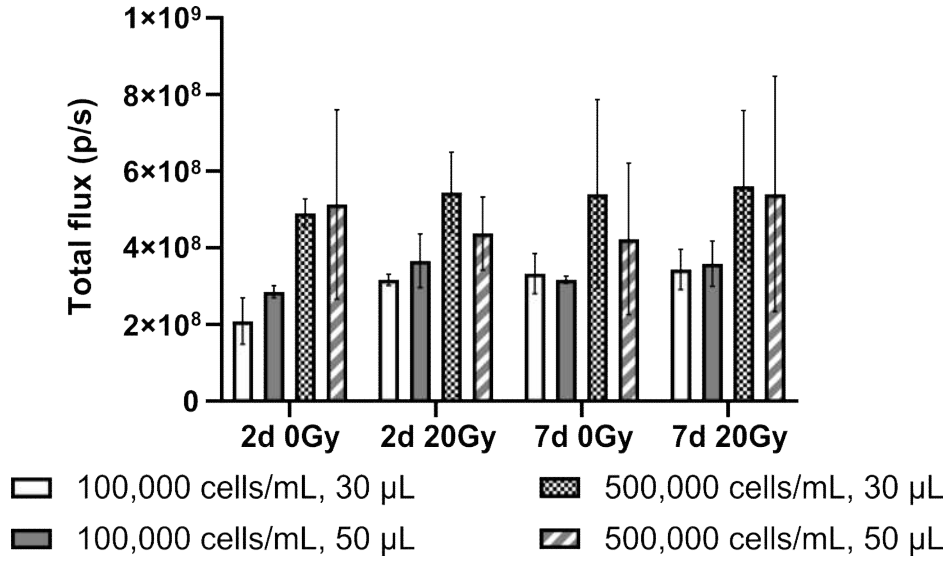

Figure 10: Bioluminescence of encapsulated 4T1 cells. Bioluminescent signal seen in GFP- and luciferase-labeled 4T1 cells at 48 hours after gelation. Error bars represent SD. N = 3.

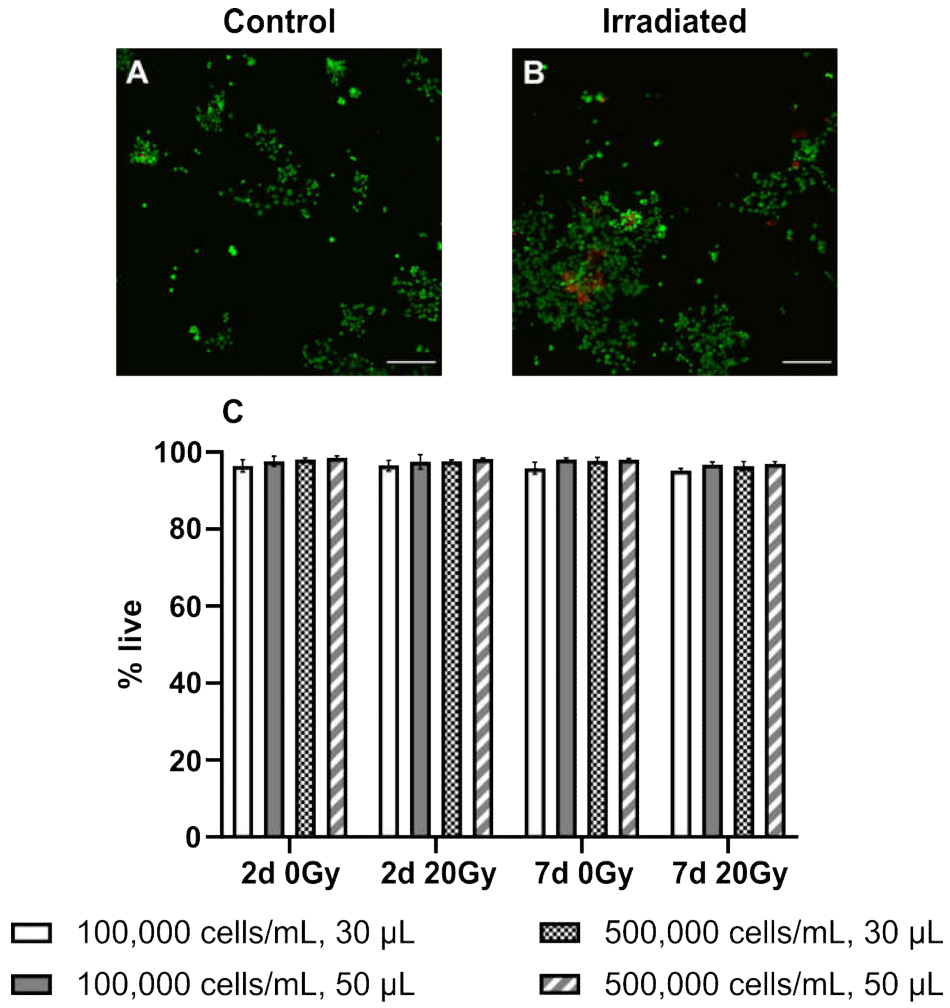

Figure 11: Cell viability. Viability assay performed on unlabeled 4T1 cells at 48 hours after gelation. Representative images of live (green, A) and dead (red, B) cells in control and irradiated conditions. Quantification of fluorescent staining (C). Scale bars: 200 µm. Error bars represent SD. N = 3.

Staining of F-actin revealed a similar cytoskeleton structure across all conditions (Figure 12). Quantitatively, anisotropic measurements indicated that hydrogels seeded at the highest cell concentration and the largest volume consistently showed increased alignment when MFPs were irradiated regardless of incubation time (Figure 13). The same increase was seen in the hydrogels

fabricated using a lower volume but seeded at the same concentration but only when MFPs were incubated for 7 days. Among the hydrogels seeded at the lower concentration, changes in anisotropy did not consistently follow changes in seeding volume or radiation exposure.

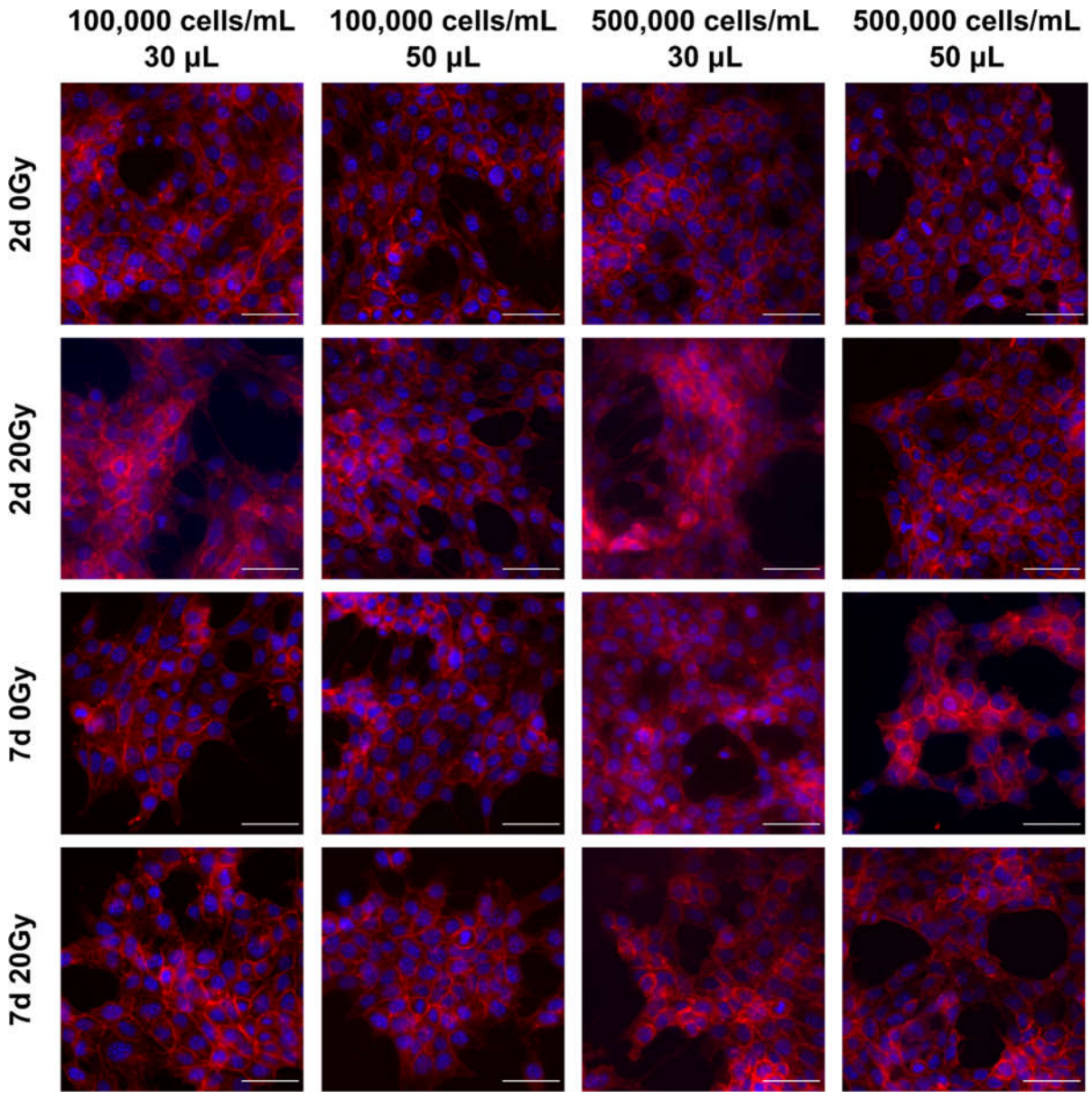

Figure 12: F-actin of 4T1 cells in hydrogels. Representative images of GFP- and luciferase-labeled 4T1 cells stained 48 hours after gelation. Phalloidin conjugate stained F-actin (red) and Hoechst 33342 stained nuclei (blue). Scale bars: 50 µm. N = 1.

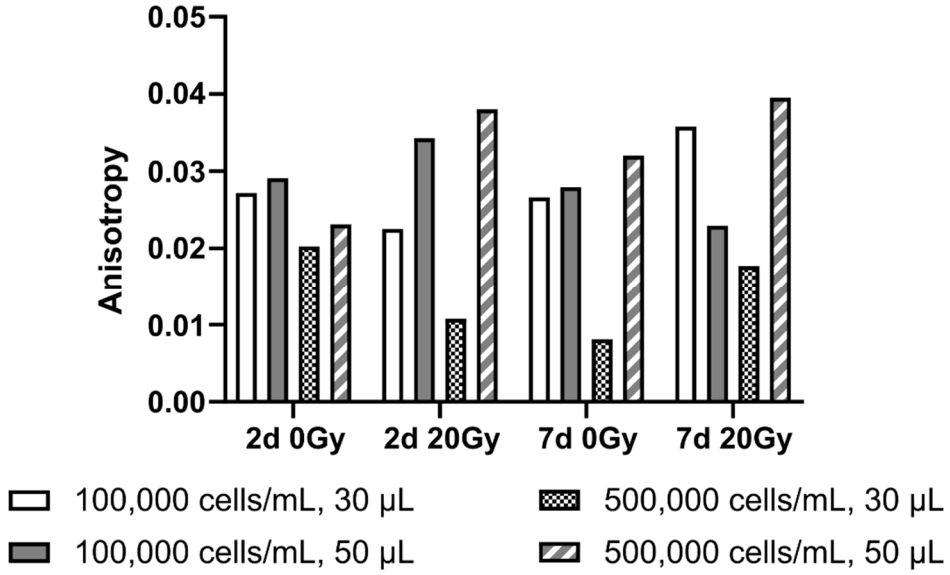

Figure 13: F-actin alignment. Anisotropy of F-actin within GFP- and luciferase-labeled 4T1 cells stained 48 hours after gelation. N = 1.

Discussion

Although some interesting trends were observed, the hydrogel system requires further development to better model the effects of radiation-induced recurrence. Differences in proliferation were not significant after 48 hours using the two concentrations of 100,000 cells/mL and 500,000 cells/mL of pregel (Figure 9 and Figure *10*). While not statistically significant, an increasing trend in bioluminescence was seen in response to radiation damage in the 2-day incubation condition when hydrogels were seeded at the lower concentration. This may indicate that the irradiated ECM produced an environment conducive to tumor cell survival, though future studies are needed for confirmation. For all radiation exposure and incubation conditions, the hydrogels seeded with a lower cell concentration had less variability than those

seeded at a higher concentration. F-actin staining revealed interesting differences in cytoskeletal alignment that were dependent on radiation dose as well as cell density (Figure 12). An increasing trend was seen in response to radiation regardless of incubation time for all hydrogels seeded at a higher cell concentration but only when seeded in a larger volume (Figure 13). This suggests that the irradiated ECM may influence tumor cell invasion and migration properties.

No hydrogel formulation was cytotoxic to 4T1 cells (Figure 11). Higher ECM concentrations within the pregel may make radiation and incubation time differences more apparent, which will be explored in future studies. Since adipose tissue is largely composed of large adipose cells, the ECM is less abundant in a given volume compared to other tissues. The 1% w/v ECM powder in pregel solution used in the current hydrogels was largely based on reported decellularization protocols of porcine adipose tissue and human lipoaspirate[71, 80]. A limitation in making the current hydrogels was the small size of MFPs, which created challenges in producing enough material. Obtaining more starting material would allow for testing of more concentrated hydrogels so as to see an impact on cell behavior in response to radiation and incubation.

CHAPTER IV

Conclusion

Summary

TNBC is an aggressive disease, and the ECM of breast tissue may play an important role in radiation-induced recurrence. Lumpectomy followed by radiation is a common form of treatment for TNBC patients, but it has been recently shown that radiation can cause CTCs to return to the primary tumor site[78]. The ECM in the irradiated area is damaged along with the cells, and changes in the ECM play an important role in recurrence. Collagen I, collagen IV, fibronectin, and laminin are major components of breast tissue ECM that likely change in response to radiation. The abundance of collagen I has made it a commonly used matrix for use in hydrogels to study tissue dynamics, but that matrix excludes all other ECM components. ECM hydrogels are the most promising option for recapitulating the environment seen by non-tumor and tumor cells. Several adipose ECM models exist, but most are based on porcine adipose tissue or human lipoaspirate. Developing a murine adipose ECM model capable of mimicking cell-matrix interactions of irradiated tissue was the goal of this work. A murine adipose ECM model is needed because it is directly relevant to much of the literature that conducts *in vivo* testing in mice, which will enable better translation to future *in vivo* studies.

Characterization of the model ECM hydrogels developed revealed physical traits similar to those in the literature for slightly different models. The decellularization process proved effective based on histological staining despite the apparent deformities. Morphologically, the ECM hydrogels appeared similar to other ECM hydrogels derived from non-murine adipose

tissue, and rheological testing confirmed that gelation was occurring in these hydrogels. However, major ECM components did not significantly change as a function of radiation damage or incubation time, nor did the alignment of the ECM. Despite the similarities in ECM composition and alignment across conditions, this characterization validates the decellularization method based on histology and rheology. The protocol was developed to be gentler than some previously published methods that were comprised of fewer steps that usually caused more damage than the steps used in the present protocol.

While our *in vitro* analysis of cell-matrix interactions revealed few statistically significant differences in proliferation or alignment, interesting trends were observed. Based on irradiation conditions and cell density, increasing proliferation trends were seen in irradiated ECM hydrogels. This indicates that the irradiated microenvironment may be conducive to tumor cell survival. In addition, F-actin anisotropy analysis revealed that fiber alignment was enhanced in irradiated ECM hydrogels depending on incubation time and density, which suggests that the irradiated ECM may influence tumor cell invasive properties. To confirm these observations, future studies are necessary to increase the number of biological replicates given the inherent variability in these experiments. In addition, the loss of material after every processing step limited our IHC and imaging surface areas, reducing available representative areas for analysis. Taken together, these results demonstrate that decellularization of MFPs was possible, adipose ECM hydrogels could be formed following irradiation, and that further adjustments need to be made to elucidate differences in the hydrogels that may exist in response to radiation and incubation time. These studies will advance the understanding of why TNBC patients experience higher rates of recurrence following radiation therapy.

Future Work

The present work focused on the development of an adipose tissue ECM hydrogel capable of mimicking an *in vivo* radiation response. Future studies need to be conducted to confirm our observed trends based on *ex vivo* irradiation of the MFPs, and additional studies will translate this technique to an *in vivo* model. The decellularization protocol proved effective, but *in vitro* testing should be further developed to elucidate such a radiation response. Since it is not uncommon for ECM hydrogels to yield low stiffness and adipose tissue is already soft, the hydrogels made in the present work likely did not span a sufficient stiffness range to have a significant influence on cell behavior. Hydrogels of varying stiffness will be examined in the future to identify an ECM concentration within the pregel solution that provides relevant changes in cell behavior as seen *in vivo*.

Further analysis of the 4T1 cell cytoskeleton will be conducted with a focus on morphological changes. Cell elongation, shape, and area that are influenced by ECM and will be investigated. Invadopodia, protrusions of actin fibers from tumor cells, are an important part of cell elongation. Interactions between cells and the ECM can cause invadopodia to degrade the key ECM components investigated in the current work: collagens, fibronectin, laminin[108]. It has been recently shown that radiation exposure can enhance the degradation potential of invadopodia by increasing the activation of MMP-2, an ECM degrading enzyme[109]. ECM fiber alignment is an important factor for further investigation because the degree of fiber alignment influences the morphology of cells grown in a matrix. It has been reported that cells cultured in a heterogeneously arranged matrix grow randomly and cell cultured in an aligned matrix grow longer and in the same direction[110].

To augment IHC staining, Raman spectroscopy has the potential for more specific analysis of components within the ECM. Raman spectroscopy is a technique that relies on the photon scattering when a sample is illuminated by a monochromatic source[111]. The amount of scattering is measured as a spectrum representing the shift in emission energy compared to excitation energy. This technique is highly sensitive, identifying differences in the composition of a material based on the signatures found in the spectrum. Others have shown the potential for using Raman spectroscopy on breast tissue, including using it as a method of cancer diagnosis[112, 113]. Using Raman spectroscopy to characterize ECM hydrogels will be beneficial for a more thorough analysis of ECM compositional changes following irradiation.

Finally, second harmonic generation (SHG) is a technique that will greatly enhance the characterization of collagen fibers in decellularized tissue. SHG is a process that absorbs two identical photons at low energy and emits one photon at twice the energy, and it cannot occur on centrosymmetric materials. Collagen I has a triple helix fibrillar structure in which each fiber carries its own dipole moment, giving a constant dipole moment to the structure as a whole. SHG can take advantage of this to identify collagen I, and it can be performed on thick sections, which would be ideal based on the histology results[114]. SHG has been reported in characterizing decellularized MFPs[74], and is commonly seen to characterize collagen I hydrogels[115, 116]. Since collagen I is the most abundant component of the ECM and is known to increase in radiation-induced fibrosis[117], using SHG on ECM hydrogels will likely maintain its sensitivity for collagen I and serve as another tool for characterization.

References

1. Hanahan, D. & Weinberg, R. A. Hallmarks of cancer: The next generation. *Cell* **144**, 646–674 (2011).

2. Siegel, R. L., Miller, K. D. & Jemal, A. Cancer statistics, 2019. *CA. Cancer J. Clin.* **69**, 7–34 (2019).

3. Kumar, V. *et al.* Functional domains of the human estrogen receptor. *Cell* **51**, 941–951 (1987).

4. Horwitz, K. & McGuire, W. Estrogen Control of Progesterone Receptor in Human Breast Cancer. *J. Biol. Chem.* **253**, 2223–2228 (1978).

5. Foulkes, W. D., Smith, I. E. & Reis-Filho, J. S. Triple-Negative Breast Cancer. *N. Engl. J. Med.* **363**, 1938–1948 (2010).

6. Shah, S. P. *et al.* The clonal and mutational evolution spectrum of primary triple-negative breast cancers. *Nature* **486**, 395–399 (2012).

7. Weigelt, B., Baehner, F. L. & Reis-Filho, J. S. The contribution of gene expression profiling to breast cancer classification, prognostication and prediction: a retrospective of the last decade. *J. Pathol.* **220**, 263-280 (2009).

8. Bianchini, G., Balko, J. M., Mayer, I. A., Sanders, M. E. & Gianni, L. Triple-negative breast cancer: challenges and opportunities of a heterogeneous disease. *Nat. Rev. Clin. Oncol.* **13**, 674–690 (2016).

9. Venkitaraman, A. R. Linking the Cellular Functions of BRCA Genes to Cancer Pathogenesis and Treatment. *Annu. Rev. Pathol. Mech. Dis.* **4**, 461–487 (2009).

10. Carey, L. A. *et al.* The Triple Negative Paradox: Primary Tumor Chemosensitivity of Breast Cancer Subtypes. *Clin. Cancer Res.* **13**, 2329–2334 (2007).

11. Hagiwara, H. & Sunada, Y. Mechanism of taxane neurotoxicity. *Breast Cancer* **11**, 82–85 (2004).

12. Gewirtz, D. A critical evaluation of the mechanisms of action proposed for the antitumor effects of the anthracycline antibiotics adriamycin and daunorubicin. *Biochem. Pharmacol.* **57**, 727–741 (1999).

13. Angsutararux, P., Luanpitpong, S. & Issaragrisil, S. Chemotherapy-Induced Cardiotoxicity: Overview of the Roles of Oxidative Stress. *Oxid. Med. Cell. Longev.* **2015**, 1–13 (2015).

14. Poggio, F. *et al.* Platinum-based neoadjuvant chemotherapy in triple-negative breast cancer: a systematic review and meta-analysis. *Ann. Oncol.* **29**, 1497–1508 (2018).

15. Robson, M. *et al.* Olaparib for Metastatic Breast Cancer in Patients with a Germline BRCA Mutation. *N. Engl. J. Med.* **377**, 523–533 (2017).

16. Loi, S. *et al.* RAS/MAPK Activation Is Associated with Reduced Tumor-Infiltrating Lymphocytes in Triple-Negative Breast Cancer: Therapeutic Cooperation Between MEK and PD-1/PD-L1 Immune Checkpoint Inhibitors. *Clin. Cancer Res.* **22**, 1499–1509 (2016).

17. Lee, J. J., Loh, K. & Yap, Y.-S. PI3K/Akt/mTOR inhibitors in breast cancer. *Cancer Biol. Med.* **12**, 342–354 (2015).

18. Miller, K. D. *et al.* Cancer treatment and survivorship statistics, 2016. *CA. Cancer J. Clin.* **66**, 271–289 (2016).

19. Whelan, T. J. *et al.* Long-Term Results of Hypofractionated Radiation Therapy for Breast Cancer. *N. Engl. J. Med.* **362**, 513–520 (2010).

20. Lowery, A. J., Kell, M. R., Glynn, R. W., Kerin, M. J. & Sweeney, K. J. Locoregional recurrence after breast cancer surgery: a systematic review by receptor phenotype. *Breast Cancer Res. Treat.* **133**, 831–841 (2012).

21. McGuire, A., Lowery, A. J., Kell, M. R., Kerin, M. J. & Sweeney, K. J. Locoregional Recurrence Following Breast Cancer Surgery in the Trastuzumab Era: A Systematic Review by Subtype. *Ann. Surg. Oncol.* **24**, 3124–3132 (2017).

22. Kim, M. Y. *et al.* Tumor Self-Seeding by Circulating Cancer Cells. *Cell* **139**, 1315–1326 (2009).

23. Wallwiener, M. *et al.* The prognostic impact of circulating tumor cells in subtypes of metastatic breast cancer. *Breast Cancer Res. Treat.* **137**, 503–510 (2013).

24. Bidard, F.-C. *et al.* Clinical validity of circulating tumour cells in patients with metastatic breast cancer: a pooled analysis of individual patient data. *Lancet Oncol.* **15**, 406–414 (2014).

25. Land, C. E. *et al.* Breast Cancer Risk From Low-Dose Exposures to Ionizing Radiation: Results of Parallel Analysis of Three Exposed Populations of Women. *JNCI J. Natl. Cancer Inst.* **65**, 353–376 (1980).

26. Leitinger, B. & Hohenester, E. Mammalian collagen receptors. *Matrix Biol.* **26**, 146–155 (2007).

27. Xian, X., Gopal, S. & Couchman, J. R. Syndecans as receptors and organizers of the extracellular matrix. *Cell Tissue Res.* **339**, 31–46 (2010).

28. Saldin, L. T., Cramer, M. C., Velankar, S. S., White, L. J. & Badylak, S. F. Extracellular matrix hydrogels from decellularized tissues: Structure and function. *Acta Biomater.* **49**, 1–15 (2017).

29. Insua-Rodríguez, J. & Oskarsson, T. The extracellular matrix in breast cancer. *Adv. Drug Deliv. Rev.* **97**, 41–55 (2016).

30. Oskarsson, T. Extracellular matrix components in breast cancer progression and metastasis. *The Breast* **22**, S66–S72 (2013).

31. Kaplan, R. N. *et al.* VEGFR1-positive haematopoietic bone marrow progenitors initiate

the pre-metastatic niche. *Nature* **438**, 820–827 (2005).

32. Gilmore, A. P., Metcalfe, A. D., Romer, L. H. & Streuli, C. H. Integrin-Mediated Survival Signals Regulate the Apoptotic Function of Bax through Its Conformation and Subcellular Localization. *J. Cell Biol.* **149**, 431–446 (2000).

33. Naba, A. *et al.* The Matrisome: In Silico Definition and In Vivo Characterization by Proteomics of Normal and Tumor Extracellular Matrices. *Mol. Cell. Proteomics* **11**, M111.014647 (2012).

34. Naba, A., Clauser, K. R., Lamar, J. M., Carr, S. A. & Hynes, R. O. Extracellular matrix signatures of human mammary carcinoma identify novel metastasis promoters. *Elife* **3**, 1–23 (2014).

35. Stratman, A. N., Malotte, K. M., Mahan, R. D., Davis, M. J. & Davis, G. E. Pericyte recruitment during vasculogenic tube assembly stimulates endothelial basement membrane matrix formation. *Blood* **114**, 5091–5101 (2009).

36. Theocharis, A. D., Skandalis, S. S., Gialeli, C. & Karamanos, N. K. Extracellular matrix structure. *Adv. Drug Deliv. Rev.* **97**, 4–27 (2016).

37. Pickup, M. W., Mouw, J. K. & Weaver, V. M. The extracellular matrix modulates the hallmarks of cancer. *EMBO Rep.* **15**, 1243–1253 (2014).

38. Liu, J. & Agarwal, S. Mechanical Signals Activate Vascular Endothelial Growth Factor Receptor-2 To Upregulate Endothelial Cell Proliferation during Inflammation. *J. Immunol.* **185**, 1215–1221 (2010).

39. Barcellos-Hoff, M. H. & Ravani, S. A. Irradiated mammary gland stroma promotes the expression of tumorigenic potential by unirradiated epithelial cells. *Cancer Res.* **60**, 1254–60 (2000).

40. O'Sullivan, B. & Levin, W. Late radiation-related fibrosis: pathogenesis, manifestations, and current management. *Semin. Radiat. Oncol.* **13**, 274–289 (2003).

41. Bernstein, E. F. *et al.* Healing Impairment of Open Wounds by Skin Irradiation. *J. Dermatol. Surg. Oncol.* **20**, 757–760 (1994).

42. Miller, N. D. & Williams, D. F. The in vivo and in vitro degradation of poly(glycolic acid) suture material as a function of applied strain. *Biomaterials* **5**, 365–368 (1984).

43. Vert, M., Li, S. & Garreau, H. New insights on the degradation of bioresorbable polymeric devices based on lactic and glycolic acids. *Clin. Mater.* **10**, 3–8 (1992).

44. Fischbach, C. *et al.* Generation of mature fat pads in vitro and in vivo utilizing 3-D long-term culture of 3T3-L1 preadipocytes. *Exp. Cell Res.* **300**, 54–64 (2004).

45. Patrick, C. W., Zheng, B., Johnston, C. & Reece, G. P. Long-Term Implantation of Preadipocyte-Seeded PLGA Scaffolds. *Tissue Eng.* **8**, 283–293 (2002).

46. Alhadlaq, A., Tang, M. & Mao, J. J. Engineered Adipose Tissue from Human Mesenchymal Stem Cells Maintains Predefined Shape and Dimension: Implications in Soft Tissue Augmentation and Reconstruction. *Tissue Eng.* **11**, 556–566 (2005).

47. Patel, P. N., Smith, C. K. & Patrick, C. W. Rheological and recovery properties of poly(ethylene glycol) diacrylate hydrogels and human adipose tissue. *J. Biomed. Mater. Res. Part A* **73A**, 313–319 (2005).

48. Pins, G. D., Collins-Pavao, M. E., Van De Water, L., Yarmush, M. L. & Morgan, J. R. Plasmin Triggers Rapid Contraction and Degradation of Fibroblast-Populated Collagen Lattices. *J. Invest. Dermatol.* **114**, 647–653 (2000).

49. Gentleman, E., Nauman, E. A., Livesay, G. A. & Dee, K. C. Collagen Composite Biomaterials Resist Contraction While Allowing Development of Adipocytic Soft Tissue In Vitro. *Tissue Eng.* **12**, 1639–1649 (2006).

50. Vashi, A. V. *et al.* Adipose Tissue Engineering Based on the Controlled Release of Fibroblast Growth Factor-2 in a Collagen Matrix. *Tissue Eng.* **12**, 3035–3043 (2006).

51. Kleinman, H. K. *et al.* Isolation and characterization of type IV procollagen, laminin, and heparan sulfate proteoglycan from the EHS sarcoma. *Biochemistry* **21**, 6188–6193 (1982).

52. Findlay, M. W. & Morrison, W. A. Tissue Engineered Breast Reconstruction. in *Breast Reconstruction* **29**, 1001–1018 (Springer International Publishing, 2016).

53. Kawaguchi, N. *et al.* De novo adipogenesis in mice at the site of injection of basement membrane and basic fibroblast growth factor. *Proc. Natl. Acad. Sci.* **95**, 1062–1066 (1998).

54. Cronin, K. J. *et al.* New Murine Model of Spontaneous Autologous Tissue Engineering, Combining an Arteriovenous Pedicle with Matrix Materials. *Plast. Reconstr. Surg.* **113**, 260–269 (2004).

55. Kelly, J. L. *et al.* Contact with Existing Adipose Tissue Is Inductive for Adipogenesis in Matrigel. *Tissue Eng.* **12**, 2041–2047 (2006).

56. Gerecht, S. *et al.* Hyaluronic acid hydrogel for controlled self-renewal and differentiation of human embryonic stem cells. *Proc. Natl. Acad. Sci.* **104**, 11298–11303 (2007).

57. Hemmrich, K. *et al.* Implantation of preadipocyte-loaded hyaluronic acid-based scaffolds into nude mice to evaluate potential for soft tissue engineering. *Biomaterials* **26**, 7025–7037 (2005).

58. Tang, S., Vickers, S. M., Hsu, H.-P. & Spector, M. Fabrication and characterization of porous hyaluronic acid–collagen composite scaffolds. *J. Biomed. Mater. Res. Part A* **82A**, 323–335 (2007).

59. Park, S.-N., Lee, H. J., Lee, K. H. & Suh, H. Biological characterization of EDC-crosslinked collagen–hyaluronic acid matrix in dermal tissue restoration. *Biomaterials* **24**, 1631–1641 (2003).

60. Campbell, J. J. *et al.* A 3-D in vitro co-culture model of mammary gland involution. *Integr. Biol. (United Kingdom)* **6**, 618–626 (2014).

61. Davidenko, N., Campbell, J. J., Thian, E. S., Watson, C. J. & Cameron, R. E. Collagen–hyaluronic acid scaffolds for adipose tissue engineering. *Acta Biomater.* **6**, 3957–3968

(2010).

62. Rowley, J. A., Madlambayan, G. & Mooney, D. J. Alginate hydrogels as synthetic extracellular matrix materials. *Biomaterials* **20**, 45–53 (1999).

63. Huebsch, N. *et al.* Harnessing traction-mediated manipulation of the cell/matrix interface to control stem-cell fate. *Nat. Mater.* **9**, 518–526 (2010).

64. Chaudhuri, O. *et al.* Extracellular matrix stiffness and composition jointly regulate the induction of malignant phenotypes in mammary epithelium. *Nat. Mater.* **13**, 970–978 (2014).

65. Pouliot, R. A. *et al.* Development and characterization of a naturally derived lung extracellular matrix hydrogel. *J. Biomed. Mater. Res. Part A* **104**, 1922–1935 (2016).

66. Bonvillain, R. W. *et al.* A Nonhuman Primate Model of Lung Regeneration: Detergent-Mediated Decellularization and Initial In Vitro Recellularization with Mesenchymal Stem Cells. *Tissue Eng. Part A* **18**, 2437–2452 (2012).

67. Crapo, P. M., Gilbert, T. W. & Badylak, S. F. An overview of tissue and whole organ decellularization processes. *Biomaterials* **32**, 3233–3243 (2011).

68. Lumpkins, S. B., Pierre, N. & McFetridge, P. S. A mechanical evaluation of three decellularization methods in the design of a xenogeneic scaffold for tissue engineering the temporomandibular joint disc. *Acta Biomater.* **4**, 808–816 (2008).

69. Seddon, A. M., Curnow, P. & Booth, P. J. Membrane proteins, lipids and detergents: not just a soap opera. *Biochim. Biophys. Acta - Biomembr.* **1666**, 105–117 (2004).

70. Faulk, D. M. *et al.* The effect of detergents on the basement membrane complex of a biologic scaffold material. *Acta Biomater.* **10**, 183–193 (2014).

71. Brown, B. N. *et al.* Comparison of Three Methods for the Derivation of a Biologic Scaffold Composed of Adipose Tissue Extracellular Matrix. *Tissue Eng. Part C Methods* **17**, 411–421 (2011).

72. Whitehead, C. M. *et al.* Exisulind-induced apoptosis in a non-small cell lung cancer orthotopic lung tumor model augments docetaxel treatment and contributes to increased survival. *Mol. Cancer Ther.* **2**, 479–88 (2003).

73. Massensini, A. R. *et al.* Concentration-dependent rheological properties of ECM hydrogel for intracerebral delivery to a stroke cavity. *Acta Biomater.* **27**, 116–130 (2015).

74. Mayorca-Guiliani, A. E. *et al.* ISDoT: in situ decellularization of tissues for high-resolution imaging and proteomic analysis of native extracellular matrix. *Nat. Med.* **23**, 890–898 (2017).

75. Keane, T. J., Swinehart, I. T. & Badylak, S. F. Methods of tissue decellularization used for preparation of biologic scaffolds and in vivo relevance. *Methods* **84**, 25–34 (2015).

76. Freytes, D. O., Martin, J., Velankar, S. S., Lee, A. S. & Badylak, S. F. Preparation and rheological characterization of a gel form of the porcine urinary bladder matrix. *Biomaterials* **29**, 1630–1637 (2008).

77. Meyer, S. R. *et al.* Comparison of aortic valve allograft decellularization techniques in the rat. *J. Biomed. Mater. Res. Part A* **79A**, 254–262 (2006).

78. Vilalta, M., Rafat, M., Giaccia, A. J. & Graves, E. E. Recruitment of Circulating Breast Cancer Cells Is Stimulated by Radiotherapy. *Cell Rep.* **8**, 402–409 (2014).

79. Rafat, M. *et al.* Macrophages Promote Circulating Tumor Cell–Mediated Local Recurrence following Radiotherapy in Immunosuppressed Patients. *Cancer Res.* **78**, 4241–4252 (2018).

80. Young, D. A., Ibrahim, D. O., Hu, D. & Christman, K. L. Injectable hydrogel scaffold from decellularized human lipoaspirate. *Acta Biomater.* **7**, 1040–1049 (2011).

81. Cebotari, S. *et al.* Use of Fresh Decellularized Allografts for Pulmonary Valve Replacement May Reduce the Reoperation Rate in Children and Young Adults: Early Report. *Circulation* **124**, S115–S123 (2011).

82. Song, J. J. & Ott, H. C. Organ engineering based on decellularized matrix scaffolds. *Trends Mol. Med.* **17**, 424–432 (2011).

83. Cortiella, J. *et al.* Influence of Acellular Natural Lung Matrix on Murine Embryonic Stem Cell Differentiation and Tissue Formation. *Tissue Eng. Part A* **16**, 2565–2580 (2010).

84. Pati, F. *et al.* Printing three-dimensional tissue analogues with decellularized extracellular matrix bioink. *Nat. Commun.* **5**, 3935 (2014).

85. Young, D. A., Choi, Y. S., Engler, A. J. & Christman, K. L. Stimulation of adipogenesis of adult adipose-derived stem cells using substrates that mimic the stiffness of adipose tissue. *Biomaterials* **34**, 8581–8588 (2013).

86. O'Neill, J. D. *et al.* Decellularization of Human and Porcine Lung Tissues for Pulmonary Tissue Engineering. *Ann. Thorac. Surg.* **96**, 1046–1056 (2013).

87. Reing, J. E. *et al.* The effects of processing methods upon mechanical and biologic properties of porcine dermal extracellular matrix scaffolds. *Biomaterials* **31**, 8626–8633 (2010).

88. Prasertsung, I., Kanokpanont, S., Bunaprasert, T., Thanakit, V. & Damrongsakkul, S. Development of acellular dermis from porcine skin using periodic pressurized technique. *J. Biomed. Mater. Res. Part B Appl. Biomater.* **85B**, 210–219 (2008).

89. Flynn, L. E. The use of decellularized adipose tissue to provide an inductive microenvironment for the adipogenic differentiation of human adipose-derived stem cells. *Biomaterials* **31**, 4715–4724 (2010).

90. Yan, H. J. *et al.* Synthetic design of growth factor sequestering extracellular matrix mimetic hydrogel for promoting in vivo bone formation. *Biomaterials* **161**, 190–202 (2018).

91. Gibbs, D. A., Merrill, E. W., Smith, K. A. & Balazs, E. A. Rheology of hyaluronic acid. *Biopolymers* **6**, 777–791 (1968).

92. Deng, A., Kang, X., Zhang, J., Yang, Y. & Yang, S. Enhanced gelation of chitosan/β-

sodium glycerophosphate thermosensitive hydrogel with sodium bicarbonate and biocompatibility evaluated. *Mater. Sci. Eng. C* **78**, 1147–1154 (2017).

93. Taherian, A. R. *et al.* Rheological and thermogelling properties of commercials chitosan/β-glycerophosphate: Retention of hydrogel in water, milk and UF-milk. *Food Hydrocoll.* **63**, 635–645 (2017).

94. Chen, Y. *et al.* A supramolecular hydrogel for spatial-temporal release of auxin to promote plant root growth. *Chem. Commun.* **54**, 11721–11724 (2018).

95. Link, P. A., Pouliot, R. A., Mikhaiel, N. S., Young, B. M. & Heise, R. L. Tunable Hydrogels from Pulmonary Extracellular Matrix for 3D Cell Culture. *J. Vis. Exp.* 1–9 (2017).

96. Boudaoud, A. *et al.* FibrilTool, an ImageJ plug-in to quantify fibrillar structures in raw microscopy images. *Nat. Protoc.* **9**, 457–463 (2014).

97. Hynes, R. O. The Extracellular Matrix: Not Just Pretty Fibrils. *Science.* **326**, 1216–1219 (2009).

98. Kaushik, S., Pickup, M. W. & Weaver, V. M. From transformation to metastasis: deconstructing the extracellular matrix in breast cancer. *Cancer Metastasis Rev.* **35**, 655–667 (2016).

99. Wicha, M. S., Liotta, L. A., Vonderhaar, B. K. & Kidwell, W. R. Effects of inhibition of basement membrane collagen deposition on rat mammary gland development. *Dev. Biol.* **80**, 253–266 (1980).

100. Schedin, P. & Keely, P. J. Mammary Gland ECM Remodeling, Stiffness, and Mechanosignaling in Normal Development and Tumor Progression. *Cold Spring Harb. Perspect. Biol.* **3**, a003228 (2011).

101. Lartey, F. M. *et al.* Dynamic CT imaging of volumetric changes in pulmonary nodules correlates with physical measurements of stiffness. *Radiother. Oncol.* **122**, 313–318 (2017).

102. Katira, P., Bonnecaze, R. T. & Zaman, M. H. Modeling the Mechanics of Cancer: Effect of Changes in Cellular and Extra-Cellular Mechanical Properties. *Front. Oncol.* **3**, 1–7 (2013).

103. Rodemann, H. P. & Bamberg, M. Cellular basis of radiation-induced fibrosis. *Radiother. Oncol.* **35**, 83–90 (1995).

104. Jacobson, L. K., Johnson, M. B., Dedhia, R. D., Niknam-Bienia, S. & Wong, A. K. Impaired wound healing after radiation therapy: A systematic review of pathogenesis and treatment. *JPRAS Open* **13**, 92–105 (2017).

105. Liu, X. *et al.* Stretchable living materials and devices with hydrogel–elastomer hybrids hosting programmed cells. *Proc. Natl. Acad. Sci.* **114**, 2200–2205 (2017).

106. Neto, A. I. *et al.* Fabrication of Hydrogel Particles of Defined Shapes Using Superhydrophobic-Hydrophilic Micropatterns. *Adv. Mater.* **28**, 7613–7619 (2016).

107. Papadopoulos, N. G. *et al.* An improved fluorescence assay for the determination of lymphocyte-mediated cytotoxicity using flow cytometry. *J. Immunol. Methods* **177**, 101–111 (1994).

108. Stylli, S. S., Kaye, A. H. & Lock, P. Invadopodia: At the cutting edge of tumour invasion. *J. Clin. Neurosci.* **15**, 725–737 (2008).

109. Mao, L. *et al.* Enhancement of invadopodia activity in glioma cells by sublethal doses of irradiation and temozolomide. *J. Neurosurg.* **129**, 598–610 (2018).

110. Dado, D. & Levenberg, S. Cell–scaffold mechanical interplay within engineered tissue. *Semin. Cell Dev. Biol.* **20**, 656–664 (2009).

111. Movasaghi, Z., Rehman, S. & Rehman, I. U. Raman Spectroscopy of Biological Tissues. *Appl. Spectrosc. Rev.* **42**, 493–541 (2007).

112. Feld, M. S. *et al.* Diagnosing breast cancer by using Raman spectroscopy. *Proc. Natl. Acad. Sci.* **102**, 12371–12376 (2005).

113. Depciuch, J. *et al.* Application of Raman Spectroscopy and Infrared Spectroscopy in the Identification of Breast Cancer. *Appl. Spectrosc.* **70**, 251–263 (2016).

114. Robinson, B. K., Cortes, E., Rice, A. J., Sarper, M. & del Río Hernández, A. Quantitative analysis of 3D extracellular matrix remodelling by pancreatic stellate cells. *Biol. Open* **5**, 875–882 (2016).

115. Hwang, Y.-J., Larsen, J., Krasieva, T. B. & Lyubovitsky, J. G. Effect of Genipin Crosslinking on the Optical Spectral Properties and Structures of Collagen Hydrogels. *ACS Appl. Mater. Interfaces* **3**, 2579–2584 (2011).

116. Paesen, R., Sanen, K., Smisdom, N., Michiels, L. & Ameloot, M. Polarization second harmonic generation by image correlation spectroscopy on collagen type I hydrogels. *Acta Biomater.* **10**, 2036–2042 (2014).

117. Yarnold, J. & Vozenin Brotons, M.-C. Pathogenetic mechanisms in radiation fibrosis. *Radiother. Oncol.* **97**, 149–161 (2010).